‘Validation of synthetic CT-based 3D-printed patient-specific saw guides for lower arm osteotomy’

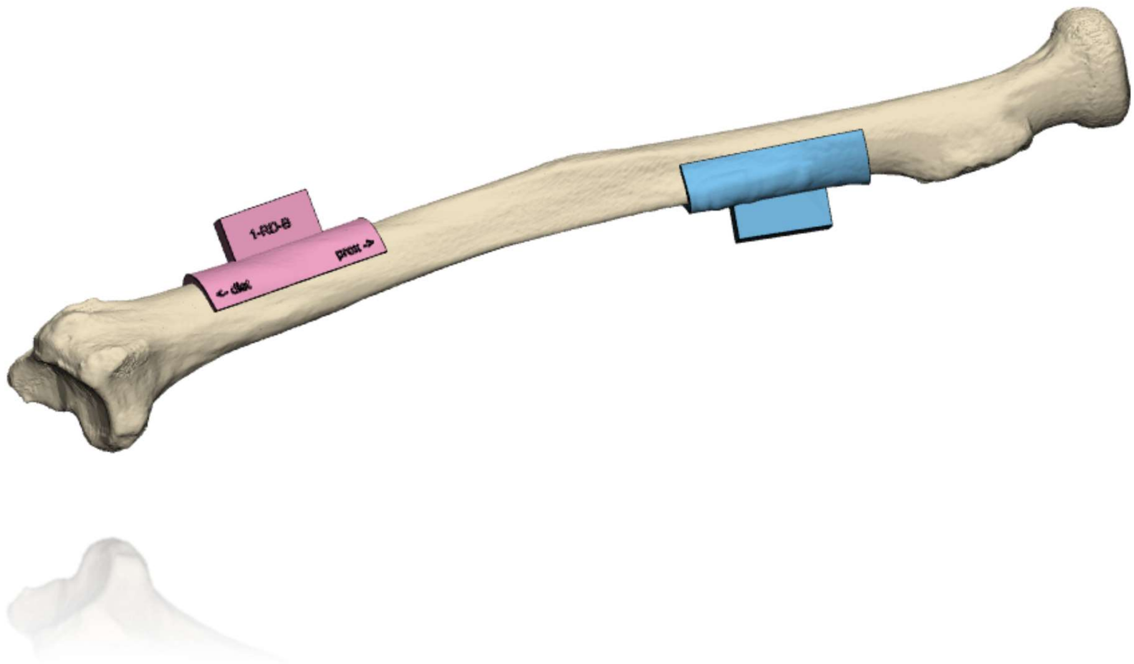

Mirte Ketel

Master thesis Technical Medicine

Faculty of Science and Technology, University of Twente

Department of Orthopedics, UMC Utrecht

3-12-2019

UMC Utrecht

UNIVERSITY OF TWENTE.

Abstract

Background

Patients, mostly aged 10-16 years, with a disability of their malunion of lower arm fractures, are treated with a lower arm osteotomy. For optimal results, three-dimensional (3D) preoperative planning and 3D-printed patient-specific saw guides are used, based on the patient's CT-scan. Although the high usability, the CT'-scan radiation is harmful and if possible, should be avoided especially for young patients. This study analyzed the position accuracy of radiation free MR-imaged synthetic CT- (sCT) and CT-based lower arm osteotomy saw guides with a cadaver study.

Methods

3D-bone models from CT-, sCT- and microCT-scans of eight cadaver human lower arms (mean age: 78y) were compared with the gold standard microCT. Six blinded observers placed CT- and sCT-based saw guides on dissected radiuses and ulnas guided by a 2D-planning. Every guide had a proximal and distal clinically relevant location. Subjective grading (1-10) analyzed the guide's fitting. The guide's position, obtained with an optical 3D scanner, was compared to the microCT's planned position. Position displacement errors includes translation, rotation and a total translation (ΔT) and total rotation error (ΔR).

Results

Overall, bones on the CT- and sCT-scans are larger when compared with the microCT-scans. The average CT-fitting grade was 6.9 (SD: 0.9) and 6.3 (SD: 1.3) for sCT and the inter- and intra-observer variability had 'slight' ($\kappa = 0.154$) and 'moderate' ($\kappa = 0.442$) agreement. No significant differences between the ΔT and ΔR of the CT- and sCT-based guides were found ($p = 0.284$ and $p = 0.216$). On Bland-Altman plots the ΔT and ΔR limits of agreement (LoA) lied within the inter-observer variability LoA.

Conclusions

This research showed equivalent CT- and sCT-based saw guide displacement errors. However, only slight observer agreement on CT- and sCT-based saw guide fitting satisfaction was found. With sCT limitations solved, the clinical sCT-based guides are promising. Ultimately the sCT may be used not solely for children, but also for adults and other orthopedic guides or implants.

Clinical Relevance

Synthetic CT-based saw guides could provide radiation free patient-specific lower arm osteotomy saw guides.

Acknowledgements

A little more than seven years ago I started my study Technical Medicine at the University of Twente and with this thesis I bring this period to an end. In January I started my graduation internship at the Orthopedic department at the UMC Utrecht and I look back at a very pleasant period thanks to the aid of the following persons.

I would like to thank Bart van der Wal for helping me developing my clinical skills, stimulating thinking things through and showing me how important it can be to really listen to a patient. I appreciate the conversations we had between consults with your advises, critical opinions and funny thoughts.

Koen Willemsen for your feedback with new ideas and critical opinions. In addition, I want to thank you for your overall support and trust during this year to develop my own ideas and views. I enjoyed our collaboration and I am sure you will establish the 3D lab, where I hope we will meet again someday.

Kees Slump for your analytical diverging or converging feedback with a wink every now and then. You helped me to rethink about problems and look at more than one solution. I enjoyed our (skype) meetings, especially the meeting when you found out our new decorations at the Q-room at the UMC Utrecht.

Rian Haarman for your open guidance to help me to get to know and embrace my qualities and pitfalls. I went to our meetings with pleasure and learned the benefit of self-reflection. I hope to see you in again in the future, maybe during an event with my brother as deejay.

The researchers of the MIRROR group for providing the critical notes during the last year. Especially Harrie Weinans, Peter Seevinck, Mateusz Florkow and Ruurd Kuiper for thinking with me and helping me puzzle with statistics and MATLAB.

The medical staff of the orthopedic department in the UMC Utrecht for making it possible to see and learn about all kinds of orthopedic conditions and surgeries.

Evelien van Genugten, Jurre Klaassen and Nynke Wijbenga for not only listening and providing feedback, but also for the fun moments we had.

My colleague researchers at Q for all the coffee breaks, the discussion and fun trips we made. I will not forget the nerf-battles, bowl champion and beautiful decoration on the blinds.

And last but certainly not least my friends and family for supporting me during the year and always being there for me!

Graduation committee:

Chairmen:	Prof. Dr. Ir. C.H. Slump[1]
Medical supervisor:	Dr. B.C.H. van der Wal[2]
Technical supervisor:	Prof. Dr. Ir. C.H. Slump[1]
Process supervisor:	Drs. R.J. Haarman[3]
Outside member:	Dr. Ir. F.F.J. Simonis[4]
Extra member:	K. Willemsen, MD / PhD Candidate[2]

1. University of Twente, Department of Robotics and Mechatronics, Enschede, The Netherlands
2. University Medical Centre Utrecht, Departments of Orthopedics, Utrecht, The Netherlands
3. University of Twente, Department of Communication and Professional Behavior, Enschede, The Netherlands
4. University of Twente, Department of Magnetic Detection & Imaging, Enschede, The Netherlands

Content

List of abbreviations and relevant definitions

3D	Three-dimensional
ALARA	As Low As Reasonably Achievable, regulation and management for ionizing radiation
AM	Additive Manufacturing, also known as 3D-printing
CT	Computed Tomography
cGAN	Conditional Generative Adversarial Network
CNN	Convolutional Neural Networks
DICOM	Digital Imaging and Communications in Medicine
DOF	Degrees Of Freedom
HU	Hounsfield Unit
ICP	Iterative Closest Point algorithm
LoA	Limits of agreement, limits to compare measurements between methods
MATLAB	Matrix LABoratory, mathematical software to analyze and calculate (ICP)-registration
MRI	Magnetic Resonance Imaging
NIfTI	Neuroimaging Informatics Technology Initiative, file format generated by the microCT
ROI	Region of interest
sCT	Synthetic Computed Tomography, based on MR-imaging
SD	Standard Deviation
STL	Stereolithography, file format for 3D reconstruction
UMCU	University Medical Center Utrecht

Concept Article: 3D-printed saw guides based on MR-imaging

Introduction

Three-dimensional (3D) preoperative planning and 3D-printed patient-specific implants and saw guides are increasingly used during orthopedic procedures. [1-3] Besides a better understanding of complex anatomies, the use of 3D-printing during surgical procedures can decrease operating time, radiological exposure and possible leading to improved surgical results concerning the patient outcome. [4] An orthopedic surgery where a 3D planning and patient-specific saw guide are used is lower arm osteotomy. This 3D-planned corrective osteotomy shows a significant functional and clinical improvement. [5] In particular patients aged 10-16 years, with a disability of their lower arm fracture malunion, are treated with a lower arm osteotomy due to less non-operative amenability. [6] Based on the patient's computed tomography (CT) scan, a virtual 3D bone model is reconstructed. On this model, preoperative surgical measurements including the surgical cutting planes and drilling trajectories are planned and translated to a patient-specific saw guide. During surgery, this saw guide is placed onto the patient's bone to guide the orthopedic surgeon. [7, 8] For the 3D planning and saw guide design, a CT-scan is used as gold standard because of its excellent hard tissue contrast and high spatial resolution. [9] However, the CT's ionizing radiation is harmful, especially for young patients. [6] The average lower arm CT-scan radiation exposure is around 0.6 mSv. [3] Although this dose is qualified as a minor risk by the International Commission on Radiological Protection, this commission also states that exposure to children should be limited to 1 mSv/year which is exceeded with a previous CT-scan that same year. [10] In addition, research shows that even low-dose radiation increases the cancer risk in young patients and should be kept as low as possible or consider alternative procedures. [11, 12]

A radiation free alternative is Magnetic Resonance Imaging (MRI). An MRI-scan generates a 3D scan without ionizing radiation and provides additional soft tissue information. Currently, in some cases MRI-scans are used for 3D-printed saw guides, but mention the lesser bone contrast of the MRI-scan compared to the CT-scan causing more intensive labor. [13, 14] Therefore, a novel deep learning based registration program was developed in the UMC Utrecht and is further developed by spin-off company MRI Guidance: a MRI-based synthetic CT (sCT). [15] This deep learning based sCT program uses convolutional neural networks (CNN) to translate MR images into Hounsfield units (HU), see Figure 7. The CNN model is trained with acquired and registered MR- and CT images of the same subject. By distinguishing bone from other signal voids in a multi-echo gradient MR-scan, the CNN automatically detects complex structures. Eventually with the sCT and MR-scan, soft tissue and bony structure information is provided with only the patient's MR images. [16] Despite the promising results of the sCT [16], it is not clinically validated for 3D-printing. Validation of the sCT is required before clinical use, to design patient-specific saw guides.

The primary aim was to investigate whether the sCT-scan provides sufficient bone surface information to be used for 3D-printed patient-specific lower arm osteotomy saw guides. Therefore, the research question states*: 'Is the accuracy and precision of the synthetic CT, compared to the currently used CT, sufficient for 3D-printed patient-specific lower arm osteotomy saw guides?*

The hypothesis was that the sCT based would have none to minimal differences from the CT. By using the sCT-scan, ionizing radiation decreases or even removes, which is especially beneficial for young patients and sufficient information to generate saw guides is provided.

Materials and Methods

To compare the sCT-scan accuracy to the currently used CT-scan for 3D-printed lower arm osteotomy saw guides, a cadaver study was executed (Figure 8). Eight healthy cadaver human lower arms (4 left and 4 right, 4 women and 4 men, mean age 78y, ranged 71-86y), obtained via Human Body Donation program of the University of Utrecht, were used.

With defrosted lower arms fixed in an extended and pronated position, a CT-scan and MRI-scan were acquired. The CT-scans (Philips Healthcare, Best, The Netherlands; 120 kV and 250 mAs) were obtained with the following parameters: 0.3 x 0.3 mm voxel spacing, 0.8 mm slice thickness and 0.4 slice spacing. The MRI-images were obtained with a 3T (Ingenia, Philips Healthcare, Best, The Netherlands) with the following parameters: 1.2 mm isotropic resolution (reconstructed to 0.6mm), 313 x 103 x 128 FOV, echo times 2.1/3.25/4.4 ms, repetition time 6.9 ms, flip angle 15, and a total scan duration of 151 seconds. With the MRI- and CT-scans, corresponding lower arms sCT-scans were generated with a 2D conditional generative adversarial network (cGAN) in Python (Python Software Foundation, Wilmington, DE, USA). As gold standard, a microCT (U-SPECT-II/CT system, MILabs, Utrecht, The Netherlands) was obtained of every bone with the following parameters: 55 KV, 0.19 mA, 75 ms exposure time and 0.05 mm reconstructed resolution. To make the bones fit in the microCT, surrounding soft tissue was dissected with standard dissection equipment (i.e. scalpels) and cut in half, see Figure 10A.

A 3D-bone model validation was performed on semi-automatic bone segmentations of the sCT-, CT- and microCT scans generated in Mimics (v21, Materialize NV, Leuven, Belgium). sCT- and CT-segmentations were created based on the thresholding method from Van den Broeck et al. [17] and the microCT with Otsu's [18] automatic thresholding based on Rovaris et al. [19]. All 3D bone models were reconstructed in Mimics (Figure 12) with the following settings: interpolation method 'contour', preferred 'continuity', shell reduction to 1, no matrix reduction applied and smoothing factor 0.3 using 2 iterations and exported as binary STL (stereolithography)-file. For an equal comparison, the 3D models were rigid registered based on the method of Van den Broeck et al. [17]. After registration, the distances between the 3D model vertices of the microCT and the sCT or CT were calculated in mm in 3-matics (v. 13, Materialize NV, Leuven, Belgium). A positive value indicates a larger sCT or CT 3D model than the microCT 3D model.

Secondly, a saw guide study was executed with saw guide designs based on clinically used lower arm osteotomy saw guides. For every radius and ulna bone, a proximal and distal guide was made (Figure 14). Based on the sCT-, CT- and microCT 3D models, 4 cm long saw guides were created in 3-matic based on the method of Caiti et al. [7] Additionally, a reference box (20 x 5 x 10 mm) was placed on top. For the corresponding sCT-, CT- and microCT-based saw guides, the box's positions were identical. A randomized letter 'A' or 'B' was added to the sCT or CT saw guide and for the microCT the 'microCT' was added (Figure 15). Per radius or ulna bone, six saw guides were generated: a proximal and distal sCT-, CT- and microCT-based saw guide with in total 96 saw guides (respectively 32 synthetic CT, 32 CT and 32 microCT saw guides) and as gold standard the microCT-based guides. 64 sCT- and CT-based guides were 3D-printed from polyamide 12 (Oceanz, Ede, The Netherlands; printing accuracy 0.12 mm in all directions). To ensure easier soft tissue removal, the cadaver bones were simmered in water (60 degrees) for 12 hours, required to obtain a 3D bone surface model with a white-light optical 3D scanner (Artec Space Spider provided by 4C, Emmen, The Netherlands; 3D resolution 0.1 mm). To analyze the simmering influence on the bones, a shrinkage analysis was conducted with a second microCT's of a selection of eight bones.

Six blinded observers (two orthopedic surgeons, two orthopedic surgeons in training and two orthopedic researchers, of which one with extensive saw guide experience) placed the 64 randomized saw guides on the corresponding bone part with the guidance of a 2D planning (Figure 16). One observer conducted the study two times on separate days, to analyze the intra observer variability. After placement, the observers were asked to grade (1-10) the saw guide's fitting satisfaction on the bone as subjective analysis.

As objective analysis, the positioning accuracy of the placed guides was measured based on the method of Caiti et al. [7]: By calculating the sCT and CT saw guides displacement, relative to the microCT saw guide positions, the position accuracy was determined. With the optical 3D scanner, 3D models of the bones with placed saw guides were created. The bones on these 3D models were rigidly registered to the bones on the microCT in MATLAB (MathWorks, Natick, USA) with an iterative closest point (ICP) algorithm [20]. After registration, with the ICP-algorithm the displacement between the sCT or CT reference boxes and the corresponding microCT box was calculated in a transformation matrix T. From this matrix, eight displacement errors were determined: three translation in the x, y and z-direction (Δx, Δy, Δz) in mm, three rotation around the x, y and z-axis (φ_x, φ_y, φ_z) in degrees and a total translation ΔT in mm and total rotational error ΔR in degrees based on Kuo et al. [21]:

$$\Delta T = \sqrt{(\Delta x)^2 + (\Delta y)^2 + (\Delta z)^2} \quad (mm)$$

$$\Delta R = \sqrt{(\varphi_x)^2 + (\varphi_y)^2 + (\varphi_z)^2} \quad (degrees)$$

Results were statistically analyzed with SPSS v. 25 (IBM Corp, Armonk, NY, USA) with in total 448 data points (7 operators x 8 lower arms x 4 halve bones x 2 guide designs). A one sample two-tailed t-test investigated whether the mean translation and rotation displacements of the sCT saw guides was equal to the mean displacements from the sCT saw guides or differ significantly. A p-value < 0.025 was considered significant. Secondly, Bland-Altman plots of the T and ΔR were created to check whether the sCT-based saw guides agree sufficiently with the CT-based saw guides. For this, two types of limits of agreement (LoA) were calculated and displayed: 1.96×SD of the intra- and inter-observer variability, with the inter-observer variability as the maximum difference. If 95% of the data of the ΔT and ΔR lies within the calculated LoA, the displacement errors of the CT- and sCT-based saw guides can be seen as equivalent. Thirdly, box plots were created to analyze differences between saw guide locations.

Results

Bone surface differences of the 3D model validation are displayed in Table 1 and Figure 22. Outliers are frequently seen at the proximal and distal bone ends (Figure 22, blue). Furthermore, the average volume difference between the pre- and poststudy microCT was -0.043 +/- 0.124 mm (mean +/- SD) (Table 2).

Subjective analysis

The average fitting grade for the CT-based saw guides was 6.9 (SD: 0.9) and for sCT-based 6.3 (SD: 1.3), see Figure 26. In addition, the average grade for proximal and distal radius saw guides were 7.1 (SD: 1.5) and 6.5 (SD: 1.7) and for proximal and distal ulna saw guides were 6.9 (SD: 1.5) and 5.8 (SD: 2.2). Furthermore, the inter- and intra-observer variability for all saw guide grades was respectively 'slight' (κ = 0.154) and 'moderate' (κ =0.442) agreement.

Objective analysis

Table 3 shows the average translation and rotation errors of the CT- and sCT-based saw guides. The largest errors are seen in the z-direction and around the z-axis (Figure 21). In addition, the one sample t-test ($p < 0.025$ significant) provided a p-value of 0.284 for ΔT and 0.216 for ΔR.

Bland-Altman plots containing the average differences between the CT and sCT-based saw guide ΔT and ΔR can be seen in Figure 27 and Figure 28. As LoA $1.96 \times SD$ of the intra- and inter-observer variability are displayed. For both the translation and rotation, the values fall between the inter-observer variability LoA.

Saw guide location error differences are distinguished in Figure 29. For both designs, distally the translation displacement and proximally the rotation displacement are the lowest. Figure 29C and D show that the translation and rotation displacements are the largest in the z-direction for both designs.

Table 4 and Figure 30 show expertise influence on the ΔT and ΔR. Observer 1 and 4 are orthopedic surgeons, observes 5 and 6 are orthopedic surgeons in training and observer 2 and 3 are orthopedic researchers, where observer 3 has extensive saw guide experience. The average execution time was 69 minutes (SD: +/- 30 min), with a maximum of 120 min (observer 3) and minimum of 40 min (observer 6).

Furthermore, in total eight percent (59/768, 64 saw guides x 6 observers x 2 errors) outliers are found (* in Figure 30). Of these outliers, 81 percent (48/59) are ulna saw guides and 73 percent (43/59) are distal located ulna saw guides.

Discussion

The one sample t-test showed no significant difference between the total translation and total rotation displacement of the CT- and sCT-based saw guides. Second, Bland-Altman plots of the total rotation and total translation displacement (Figure 27 and Figure 28) show that the LoA of these displacements lie within the LoA of the inter-observer variability. This implies that, despite initial resolution differences, displacement differences of the CT- and sCT-based saw guides are equivalent.

When comparing the study results to comparable publications, some noteworthy are found. Caiti et al. [7] analyzed positioning errors of distal, mid-shaft and proximal radius saw guides. They showed that distal guides have the smallest total translation (ranged 0.25-1.8 mm) and rotation (ranged 0.2-1.6 degrees) errors when compared to proximal (respectively ranged 0.15-2.25 mm and 0.3-5.7 degrees) or mid-shaft guides (respectively ranged 0.4-3.2 mm and 1.3-7.3 degrees). These values are lower than the results of this study (Figure 29), which can be explained by several aspects. First of all, Caiti et al. used 3D-printed radius bones, while this study used real cadaveric radius and ulna bones to mimic clinical practice. Secondly, different anatomical locations were used: Caiti et al. investigated three locations (distal, proximal and mid-shaft) on only radius bones, while this study focused on two locations (distal and proximal) for both radius and ulna bones. Thirdly, different saw guide lengths were used: The guides of this study had a length of 4 cm, while the guides of Caiti et al. were minimal 5 cm. With a longer length, the saw guide may have more anchors to hang on to and thus smaller displacements.

The shrinkage analysis with the second microCT's, an average shrinkage of 0.043 mm (Table 2) was seen, less than the 0.5 mm boiling shrinkage from literature [22] and microCT resolution. Therefore, this shrinkage had minimal to no influence on the saw guide placement.

A limitation is the interpretation of the study to a clinical outcome of a lower arm osteotomy. The results show displacement errors, where a larger displacement indicates a less accurate cutting plane compared to the planning. Ma et al. [23] showed the clinical relevance of distal radius osteotomy guides by translating the displacement errors to correction errors of the ulnar variance, radial inclination and volar tilt. A recommendation is to compare the study results to those of Ma et al. by creating a virtual lower arm osteotomy model with the generated 3D models and apply the calculated displacement errors.

Furthermore, patients treated with lower arm osteotomy have generally more deformed bones resulting in a 'natural' fixation of saw guides. [3] The cadaver bones were less deformed resulting in less anchors, possible inducing saw guides position errors. For example, the most round and anchorless distal ulna had the lowest grades (average 5.8) and largest errors (Figure 31). A recommendation is to use 3D-printed bones from patients who are treated with lower arm osteotomy for a more realistic result.

For future use, if the sCT is proven equivalent to CT, the sCT scan could be validated with a sCT-based saw guide patient study. An important aspect to analyze is the cost-effectiveness of this method. Even though MRI does not use any radiation, MRI is costly and time-consuming. A lower arm MRI-scan required 30-60 minutes, while a CT-scan requires 15 minutes. [24, 25] Furthermore, the sCT could be validated to design and 3D-print other patient-specific saw guides and implants.

This research showed equivalent CT- and sCT-based saw guide displacement errors. However, slight observer agreement on CT- and sCT-based saw guide fitting satisfaction was found. Moreover, when sCT limitations are solved it could be clinically used. Ultimately the sCT may be used not solely for children, but also for adults and other orthopedic guides or implants.

Source of funding

No funding source played a role in this study.

1. Introduction

1.1 Clinical background

Three-dimensional (3D) preoperative planning and 3D-printed patient-specific implants and saw guides are increasingly used during orthopedic procedures. [1-3] Besides a better understanding of a complex anatomy, the use of 3D-printing during surgical procedures can decrease operating time and radiological exposure. It possibly leads to improved surgical results with respect to the patient outcome. [4] In the University Medical Center Utrecht (UMCU), patients who undergo lower arm osteotomy are treated with the aid of a 3D-planning and 3D-printed patient-specific saw guides (see Chapter 1.1.1). Other patient groups where 3D-patient-specific saw guides and implants may be beneficial are hip dysplasia and shoulder arthroplasty. Recently an old-fashioned shelf arthroplasty with a 3D-printed titanium implant was renewed for hip dysplasia patients (Appendix C.1 - Hip dysplasia). For shoulder instability a similar potential treatment is proposed (Appendix C.2 - Anterior glenohumeral instability). In addition, 3D bioprinting may provide a huge step forward in tissue engineering for anatomical defect treatments (Appendix C – Biodegradable hip/shoulder project). [26]

1.1.1 Radius and ulna corrective surgery

Most radius, ulna or antebrachii fractures are the result of a trauma and commonly seen in the emergency room. For example, for all pediatric fractures (age < 10 years), five percent is comprised of antebrachii fractures, see Figure 1. [27, 28] These posttraumatic fractures generally heal without complications. However, a malunion of these fractures can lead to permanent disability, in particular midshaft fractures with an angular deformity larger than 30 degrees. [29, 30] The disability of patients with malunion of lower arm fractures includes cosmetic problems, a painful distal radioulnar joint and a limited range of motion in pronation-supination. [31] These complications are caused by tension of the interosseous membrane and bone impingement, see Figure 2.

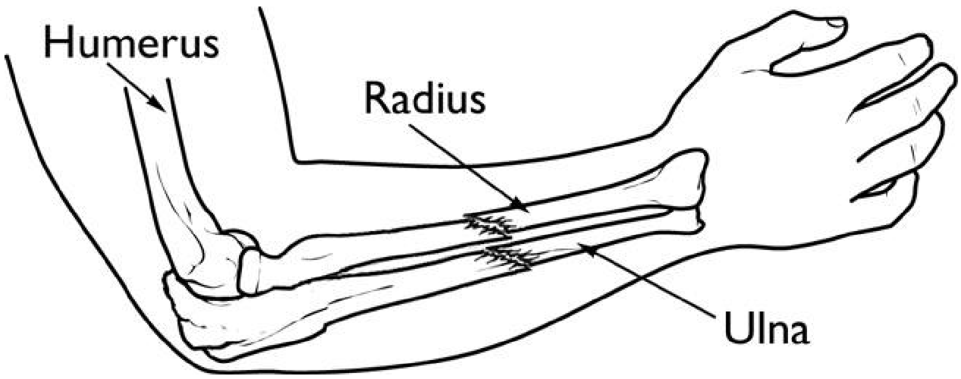

Figure 1: Right lower arms with an antebrachii fracture; both the radius and ulna bone are broken. [32]

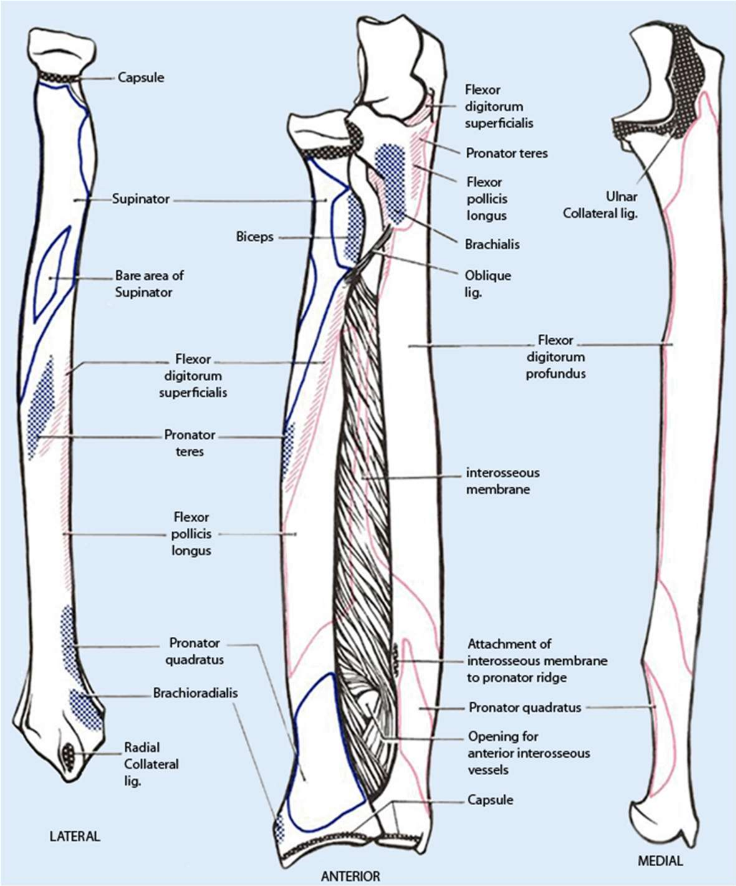

Figure 2: Radius and ulna bone with surrounding soft tissue and muscles. [33]

The majority of patients with forearm fractures are treated with closed reduction using plaster and immobilization of the lower arm with a sling. Midshaft malunions of at least 30 degrees should be surgically corrected, after soft tissue has recovered from initial immobilization. Due to skeletal maturity, forearm fractures in adolescent patients (aged 10-16 years) are less non-operative amendable then younger patients making them the largest patient group. [6] With corrective lower arm osteotomy surgery, the range of motion of the patient's lower arm is increased. Based on the patient's radiograph, a maximum plane of deformity is determined. During surgery, one or two cutting planes are applied on the radius, ulna or both with an anterior approach. The affected bone will then be realigned. If necessary, a bony wedge could be inserted or removed to correct the bone alignment (Figure 3). [30, 34, 35]

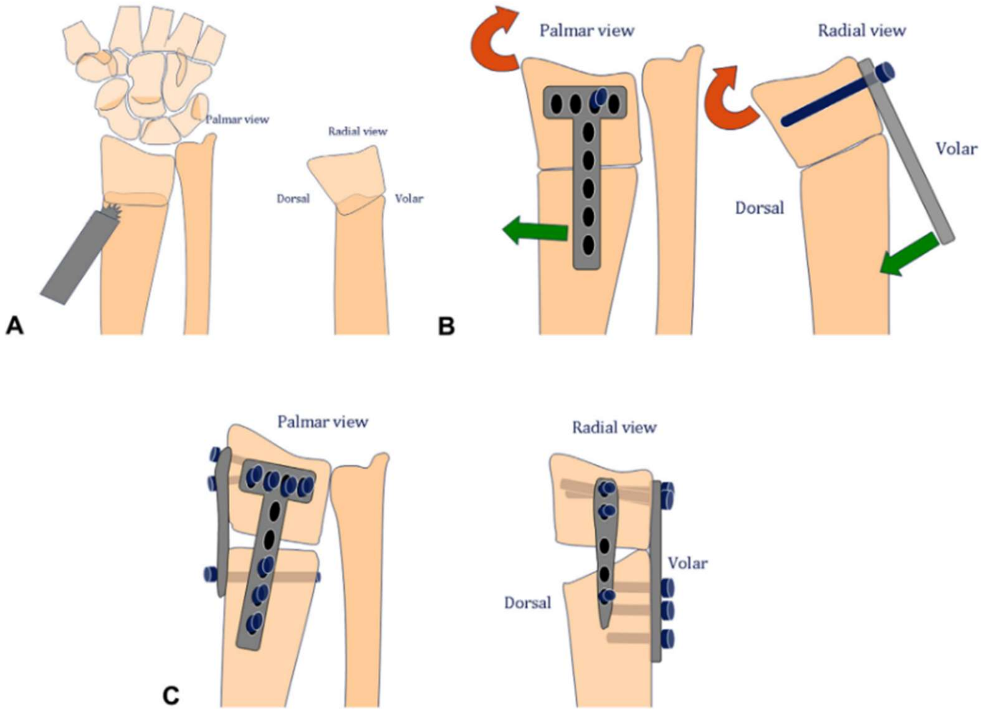

*Figure 3: Schematic distal radius osteotomy with a plate fixation. **A)** A corrective cut is made distally on the radius. **B)** First the plate is fixated distally on the radius and the proximal part can be maneuvered to create correct rotation. **C)** With screw fixation the plate is locked into place and the deformity is corrected. [36]*

1.1.2 3D planning and patient-specific saw guides/implants

The standard procedure for lower arm osteotomy uses the patient's radiograph (Figure 4) to determine the inclination angle and wedge dimension in 2D to insert into the osteotomy gap. However, if possible the planned correction will be conducted in 3D and based on the healthy contralateral lower arm to restore six parameters: three displacements and three rotations. [37] Therefore, correction ideally requires a 3D preoperative planning based on 3D acquired images and ultimately a 3D-printed patient-specific saw guide to guide cutting and drilling during surgery. A saw guide makes this procedure even less invasive, by minimizing the initial incision and mobilization of soft tissue. [3, 38] This 3D-planned corrective osteotomy shows a significant functional and clinical improvement compared to conventional standard planning methods with a radiograph. [5, 39, 40]

*Figure 4: **A)** Pre-operative patient's radiograph with an anterior posterior and lateral view of the left hand with a radial malunion radiograph. **B)** Postoperative radiograph with plate fixation. [41]*

Based on the patient's computed tomography (CT) scan, a virtual bone model is reconstructed in a 3D planning software. On this model, preoperative surgical measurements, including the surgical cutting planes and drilling trajectories, can be planned. These measurements are then translated to a patient-specific saw guide: a customized plastic 3D-printed mold featuring planned drilling holes and the planes for the osteotomy cuts (Figure 5). During surgery, this saw guide is placed onto the patient's bone to guide the orthopedic surgeon. To fit the guide on the appropriate bone location, surrounding soft tissue is dissected. However, as minimal as possible tissue is dissected to prevent nerve damage and functional loss. The saw guides are then fixated with k-wires to prevent saw guide displacement during the osteotomy cuts. A replica of the patient's bone with the saw guide placed on the correct position is 3D-printed in true size as 3D planning for the orthopedic surgeon. [7, 8, 33, 42] Research shows that patient-specific saw guides are easier in use and produce a correction that is more precise than marker-based navigation systems and in general reduce the time and radiation exposure of the operation. [23, 43]

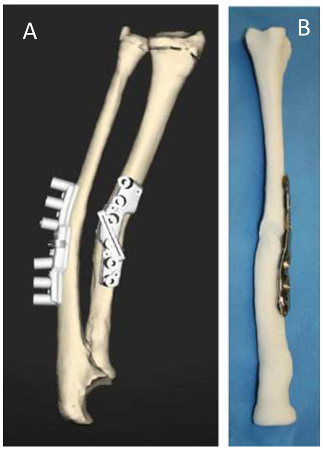

*Figure 5: **A**) Patient-specific osteotomy saw guides on an ulna and radius bone. **B**) Plate constructs on the radius bone. [42]*

1.2 Problem definition

For the 3D planning and saw guide design, a CT-scan is the gold standard due to its excellent hard tissue contrast and high spatial resolution. [9] Unfortunately during a CT-scan, patients are exposed to ionizing radiation, which is harmful for a patient's health. This holds especially true for young patients (aged < 16 years) who are the largest group of patients treated with lower arm osteotomy. [6] The average ionizing radiation exposure of a lower arm CT-scan is 0.6 mSv. [3] Although this dose is estimated as a minor risk, the exposure to children should be limited to 1 mSv/year to keep the exposure as low as reasonably achievable (ALARA). [10] Most patients already obtained a radiograph, accumulating their exposure to ionizing radiation. In addition, if patients already obtained a CT-scan that year, the ALARA limit is exceeded. Research shows that even low dose ionizing radiation increases the cancer risk in young patients, thus the ionizing radiation exposure should be kept ALARA or avoided with alternative procedures. [11, 12]

A radiation free alternative is Magnetic Resonance Imaging (MRI). An MRI-scan generates a 3D scan without ionizing radiation and provides additional soft tissue information (such as ligaments, cartilage and muscles). This additional information is helpful for the saw guide design, for example to indicate muscle insertions. Currently, some cases use MRI-scans to design 3D-printed saw guides, but mention the lesser bone contrast (when compared to the CT-scan) increasing the time and effort to design the guides. [13, 14] Therefore, based on deep learning a novel registration program was developed in the UMCU called a MR-based synthetic CT (sCT) and is further developed by spin-off company MRI Guidance. [15]

1.3 Technical background

1.3.1 Synthetic CT

Initially the synthetic CT (sCT) was developed for radiotherapy treatment planning to reduce the amount of CT- and MRI-scans. With the sCT, the need for a separate CT and multi-model registration exam are eliminated. [44] The deep learning based sCT model uses convolutional neural networks (CNN) to translate MR-images into CT Hounsfield units (HU) and the CNN model is trained with acquired and registered MR- and CT-images of the same subject (Figure 6).

Figure 6: Example of a dataset to train the synthetic CT with a multi-echo gradient MR scan and the registered CT image of the same subject, in this case the sagittal view of a left lower arm in a pronated position. [16]

By distinguishing bone from other structures in a multi-echo gradient MR-scan, the CNN automatically detects anatomical structures on the scans. Eventually with the sCT and MR-scan, information of soft tissue and bony structures is provided with only the patient's MR-images. [16] An example of a sCT-slice and the corresponding CT-slice can be seen in Figure 7. Furthermore, results from sCT models applied on various clinical data of the lower arm, head, neck, spine and pelvis show promising results. [15, 16, 45, 46]

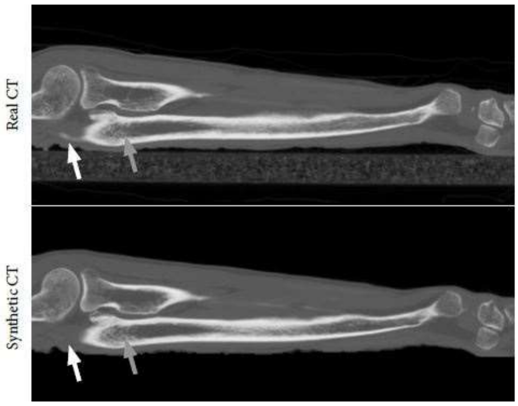

Figure 7: Sagittal view of a CT and corresponding sCT of a left lower arm (Based on the MRI-scan in Figure 6). The white arrow indicates an error in the bone shape on the sCT. The grey arrow shows internal bone structures visible on the sCT. [16]

1.3.2 3D printing

3D printing, also known as additive manufacturing (AM), is a manufacturing technology which fabricates a designed 3D model with a powder, plastic or metal material layer by layer. 3D printing can be a flexible, fast and cost-effective solution to optimize the patient's treatment. It is currently used in various medical fields, such as traumatology, tumor surgery and maxillofacial surgery. [43] In orthopedics this technique is applied to produce surgical saw guides and patient-specific implants. [47] This medical AM process can be divided in four steps. First, the anatomical region of interest (ROI) is scanned with an imaging modality, such as a CT- or MRI-scan. Next, these images are converted from a Digital Imaging and Communications in Medicine (DICOM) file to a 3D surface model in a standard tessellation language (STL) file. Then, computer aided design (CAD) is used to enhance or adjust the 3D surface model and generate the guide or implant. Finally, the desired implant or guide model is 3D-printed. Most inaccuracies in the 3D-printed model occur during the first two steps (imaging and image processing) due to noise, patient motion, beam hardening and (metal) artefacts in the used scan. In addition, the AM product accuracy is limited by the image slice thickness and slice interval of the image. [48] Research shows that patient-specific 3D-printed implants with a preoperative planning, can decrease operating time, thereby the infection risk and improve surgical cutting or drilling accuracy. [47]

1.4 Research proposal

The use of a sCT-scan based on MR-images for the design and 3D printing of patient-specific implants may be beneficial. With only a required MR-scan, the patient guarded for any harmful ionizing radiation exposure. In addition, more specific visual feedback on the soft tissue around the bones can be provided during the design of the implant, making the design process more robust.

Despite promising results of the sCT-scan, it is not clinically validated to use as input for 3D printing. Validation of the sCT-scan accuracy is required before clinical use, to safely design and 3D-print patient-specific implant and saw guides. Therefore, the research question of this thesis is:

‘*Is the accuracy of the synthetic CT-scan based on MR-images equivalent to the currently used CT-scan, to be used for 3D printing of patient-specific saw guides for lower arm osteotomy?*’

The primary aim of this thesis was to investigate whether the sCT-scan provides sufficient bone surface information to be used for 3D-printed patient-specific saw guides for young patients (aged < 16 years) treated with a lower arm osteotomy.

The hypothesis of this study is that the sCT, trained with the real CT-scan, should have none to minimal differences when compared to the real CT-scan. Therefore, none to minimal differences should be found when using the sCT as input for 3D-printed saw guides. In addition, the radiation free sCT-scan decreases or even removes harmful ionizing radiation exposure, which is especially beneficial for young patients. When the accuracy of the sCT-scan is proven sufficient, the sCT can also be applied for adult patients treated with a lower arm osteotomy or even other orthopedic guides or implants.

2. Methods

To compare the accuracy of the sCT-scan to the CT-scan for 3D printing of lower arm osteotomy saw guides, a cadaver study was executed. An overview of this study can be seen in Figure 8. This overview shows four main outcomes. First, a 3D model validation of three image modalities was carried out to (Figure 8, yellow). Second, an position accuracy analysis of 3D-printed saw guides was evaluated, with a subjective grading analysis (Figure 8, red) and an objective displacement of saw guides analysis (Figure 8, yellow). This study used eight cadaveric lower arms, which underwent several processing steps (Figure 8, blue). Of these arms, four types of scans were obtained (Figure 8, purple). For each ulna and radius, two saw guide locations were used: a proximal and distal clinically relevant location. In total, the position of 64 saw guides placed by six observers were analyzed. Lastly, to evaluate the processing steps influence on the bone surfaces a shrinkage analysis was carried out (Figure 8, purple).

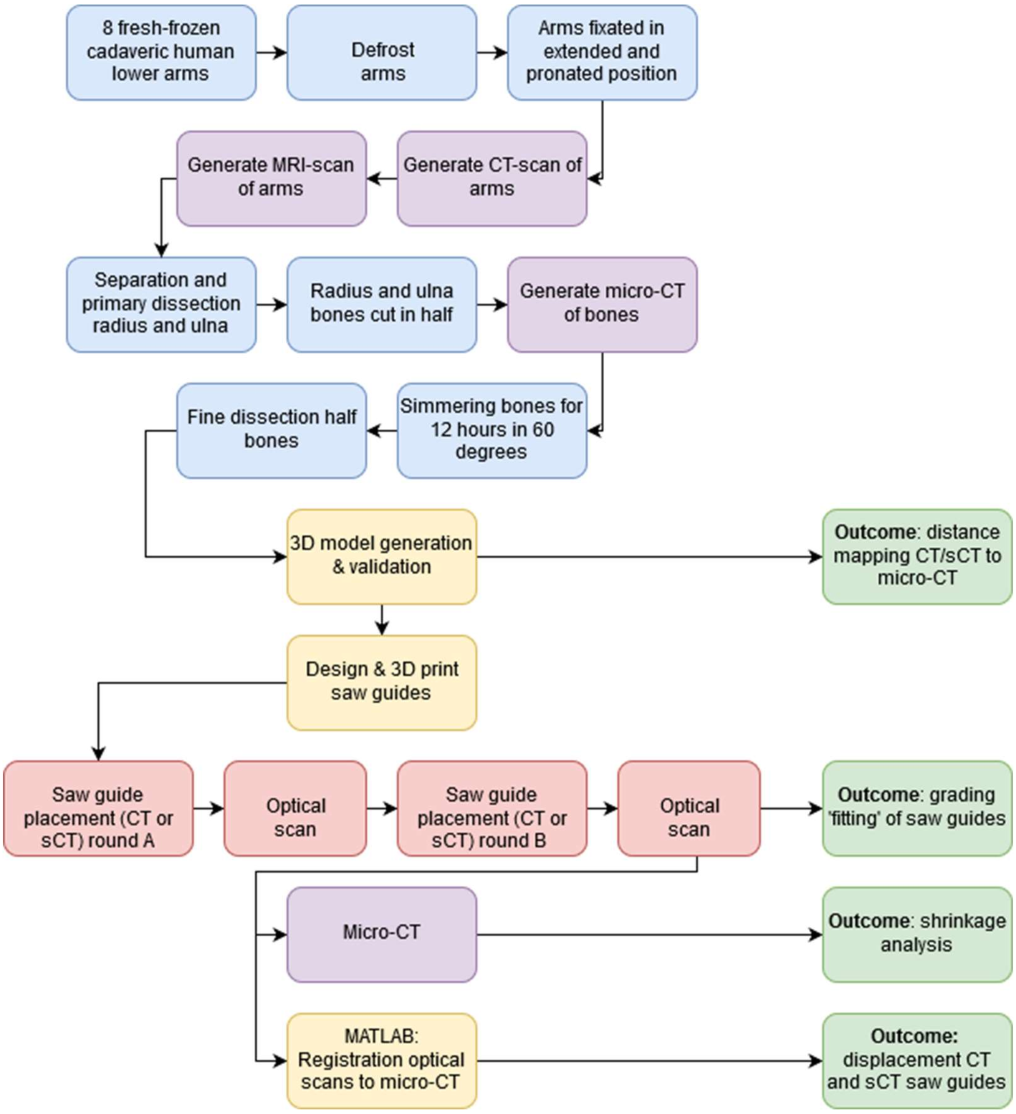

Figure 8: Overview of this study. Blue shows all processing steps of the cadaveric arms and purple all the obtained scans from the cadaveric arms. Yellow illustrates the two processing steps in 3D software and the red boxes show the saw guide study.

2.1 Materials

Eight cadaver human lower arms (four left and four right arms; four women and four men; range: 71-86 years, mean age: 78 years), obtained through the Human Body Donation program of the University of Utrecht, were used to compare two ways of lower arm osteotomy saw guides in a clinical setting. The first approach is based on the current clinical gold standard, the CT-scan. The second saw guide approach is based on a sCT-scan. Defrosted lower arms were scanned in a CT- and MRI-scan in an extended and pronated position. The arms were fixated to create identical positions in both CT- and MRI-scans (Figure 9A and B). The CT-scans (Brilliance 64, Philips Healthcare, Best, The Netherlands; 120 kV and 250 mAs) were made with a 0.3 x 0.3 mm resolution, 0.8 mm slice thickness, 0.4 mm slice spacing, 842 slices and a collimation of 64 x 0.625 mm. The MRI-scans obtained with a 3T (Ingenia, Philips Healthcare, Best, The Netherlands) were made with the following parameters: 1.2 mm isotropic resolution (reconstructed to 0.6 mm), 313 x 103 x 128 FOV, echo times 2.1/3.25/4.4 ms, repetition time 6.9 ms, flip angle 15 degrees, and a total scan duration of 151 seconds. With the MRI- and CT-scans, a corresponding sCT-scan of the lower arms were generated (Figure 9C) with a 2D conditional generative adversarial network (cGAN) in Python (Python Software Foundation, Wilmington, DE, USA).

As reference gold standard, for every bone a microCT (U-SPECT-II/CT system, MILabs, Utrecht, The Netherlands; 55 kV, 0.19 mA, exposure time 75 ms) was acquired with a reconstructed resolution of 50 micron, see Figure 9D. The microCT was chosen to obtain the highest possible bone surface accuracy, without influencing the cadaveric bone surface. An optical 3D scan was not selected as gold standard, since this image modality required removing all soft tissue that could influence the bone surface. To make the bones fit in the microCT-scanner, as much as possible soft tissue of the ulna and radius bones was removed with standard dissection equipment (i.e. scalpels) without influencing the bone surface. Finally, the bones were cut in half (Figure 10A). The final microCT scans were reconstructed from samples of six cm with the reconstruction software MILabs-Rec (MILabs, Utrecht, The Netherlands).

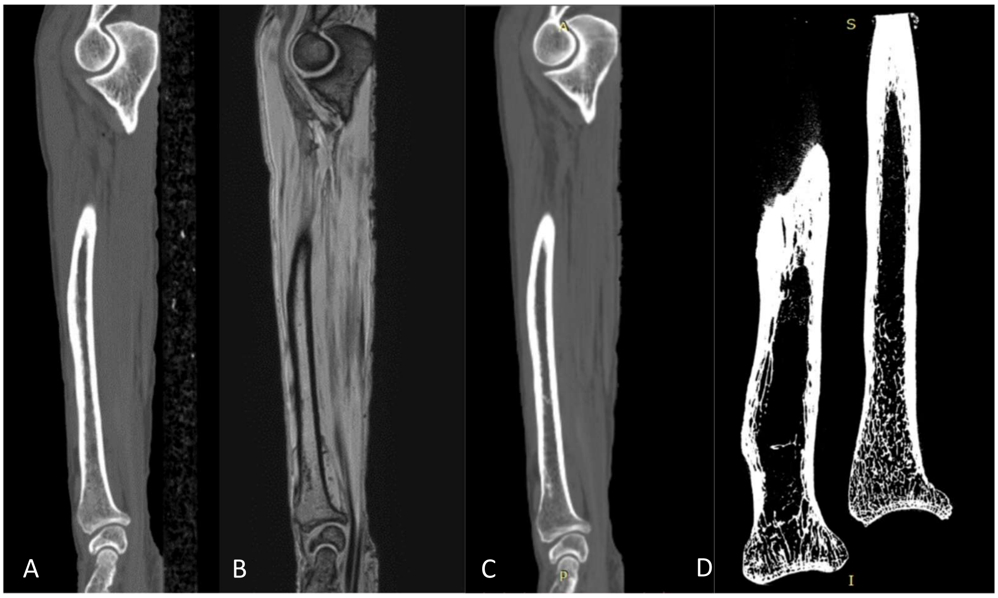

*Figure 9: **A**) The obtained CT-scan, **B**) MRI-scan, **C**) sCT-scan and **D**) microCT-scan of the same cadaveric lower arm (P1).*

After the microCT, the bones were simmered for 12 hours in water of 60 degrees Celsius to ensure an easier removal of the remaining soft tissue (Figure 10B). This process step was required for the use of the optical 3D scan to validate the saw guide placement. An optical 3D scanner generates a 3D model of surfaces, including remaining soft tissue. Soft tissue causes an inaccurate 3D model of the cadaver bone surface and eventually leading to an inaccurate registration with the 3D bone model generated from the CT- or sCT-scan. According to research, besides using a special microwave, boiling and simmering were the most effective treatment with the least influence on the cortical and trabecular bone to remove soft tissue. [49] Gelaude et al. [22] showed that boiling bones results in shrinkage of bone tissue of approximate 0.5 mm, therefore simmering was chosen to have none to minimal shrinkage. To analyze if the processing steps influenced (simmering, cutting soft tissue and dehydration) the bones, an additional microCT of a selection of eight bones was made. A distance mapping ('part comparison analysis' in 3-matic) was applied on the microCT's, similar to the 3D model validation. For a more detailed description of this method, see the section '3D model validation'.

Figure 10: ***A****) A radius (upper) and ulna (lower) bone are showed after primary dissection of the soft tissue.* ***B****) The distal radius bone part is shown after simmering and fine dissection and cutting the bone in half.*

This imaging sequence including the CT, sCT and microCT lower arm scans was chosen, since the sCT algorithm requires bones surrounded by soft tissue to generate a realistic sCT. Therefore, primary and fine dissection were applied after the MRI-scans for the microCT.

2.2 Study setup

To validate the accuracy of the sCT-scan for 3D printing of saw guides, two analysis were conducted. First a 3D model validation (2.2.1) followed by an analysis of sCT- and CT-based 3D-printed saw guides (2.2.2).

2.2.1 3D model validation

To evaluate the bone surface accuracy of the sCT-scan, compared to the CT- and microCT-scan, a 3D model validation was conducted in three consecutive steps. First, 3D bone models were generated from the three image modalities. Secondly, the 3D bone models were rigidly registered in the 3D space to each other. Finally, to analyze differences a distance mapping between the 3D models was applied.

To generate 3D bone models, radius and ulna bones were semi-automatic segmented from the sCT-, CT- and microCT-scans in Mimics (v. 21, Materialize NV, Leuven, Belgium). This method was chosen to create efficiently comparable segmentations based on the method from Van den Broeck et al. [17], who also generated corresponding 3D bone models from different image modalities to compare to each other. The generated microCT 3D models were used as 3D bone surface gold standard. With the 'CT Bone' function in Mimics, masks of the ulna and radius bones from the CT and sCT were created with grey value thresholding. HU values between 226-3071 were selected to generate comparable bone segmentations, based on the clinical HU-range of bone provided by Mimics (Figure 11A). In addition, positive seed points on the radius and ulna bones and negative seed points on the surrounding soft tissue were applied to generate the segmentations quicker and eliminate other bony structures, such as the humerus or carpal bones. To generate a solid 3D model, the bone masks were binary filled (Figure 11B). To generate the microCT 3D model, a different threshold in Mimics was applied. With the small voxel size and high exposure of the microCT, compared to the CT and sCT, the resolution and HU-values for bones were increased making the threshold of 226-3071 inaccurate to segment the bones. Based on the method from Rovaris et al. [19], the microCT-threshold was determined with Otsu's automatic thresholding [18] in the Java-based image processing program ImageJ. [50] This program was compatible with the raw microCT NIfTI-file (Neuroimaging Informatics Technology Initiative) to apply the automatic Otsu-thresholding on. With the found values in ImageJ, the segmentation was conducted in Mimics. Finally, manual mask-based adaptations were applied, including disconnecting the ulna and radius mask and completing the mask on locations with low contrast and unclear tissue delineation. For all scans, the final 3D model was constructed in Mimics with the following reconstruction settings: interpolation method 'contour', preferred 'continuity', shell reduction 1, no matrix reduction and smoothing factor 0.3 using 2 iterations. These settings caused as minimal as possible 3D model alterations. After reconstruction the 3D models were exported as binary STL-file, see Figure 12.

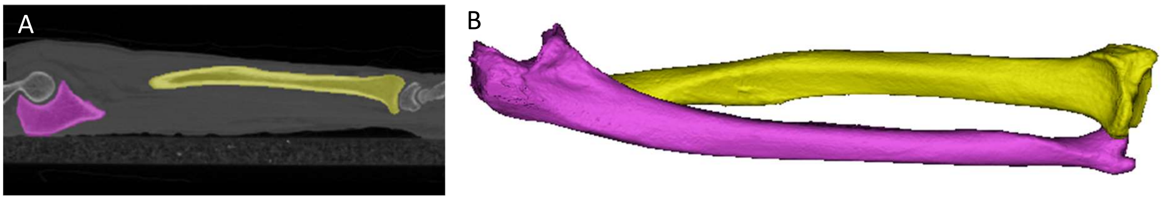

*Figure 11: **A**) The segmented radius (yellow) and ulna (purple) on a CT-scan. **B**) The corresponding 3D model of these segmentations in Mimics*

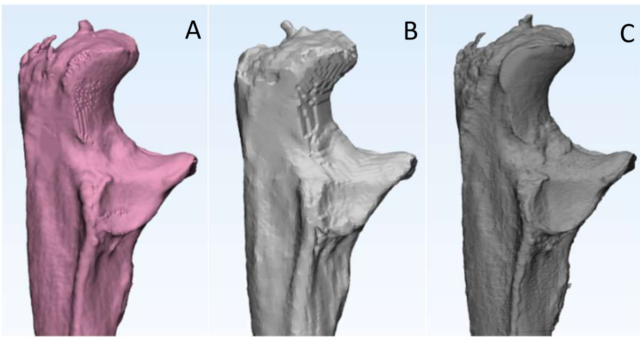

*Figure 12: 3D models of a proximal ulna with **A**) the CT-scan (pink), **B**) sCT-scan (light grey) and **C**) microCT scan (dark grey).*

To compare the generated 3D models, the sCT and microCT 3D models were rigidly registered to the corresponding CT 3D model. Initial global registration was conducted in Mimics; for the sCT with the function 'axis alignment' and for the microCT with the function 'point registration' with 10 corresponding points on both 3D models. A second rigid registration was accomplished with a Iterative Closest Point (ICP)-registration [20] in MATLAB (MathWorks, Natick, USA): by calculating the minimal distance between the two point clouds of the 3D models (sCT versus CT and microCT versus CT) the sCT and microCT were rotated and translated in six degrees of freedom (DOF) to the CT. For a detailed ICP description see section 2.3.

Distance mapping

As final step, distances between the 3D models were calculated in 3-matic (v. 13, Materialize NV, Leuven, Belgium). With the function 'part comparison analysis' a signed straight-line distance deviation between the surfaces of two corresponding 3D models were calculated. With the microCT as gold standard, the microCT 3D bone model was compared to the corresponding CT and sCT 3D bone model. For this calculation, a ROI of the 3D models was selected. With the physical cadaver bones cut in half for the microCT, the microCT 3D models consists of half bones while the CT- and sCT 3D models consists of complete bones. To exclude the physical cutting plane and bone fragments for an equal comparison, two cutting planes ('sketch plane' function) two mm from the physical cutting plane were applied in 3-matic on the 3D models (Figure 13). From these planes the rest of the 3D models was the selected ROI of the 3D models for a distance mapping. With the distance mapping, the primary objective of the 3D model validation is the measured distance between the microCT and CT/sCT scan in mm.

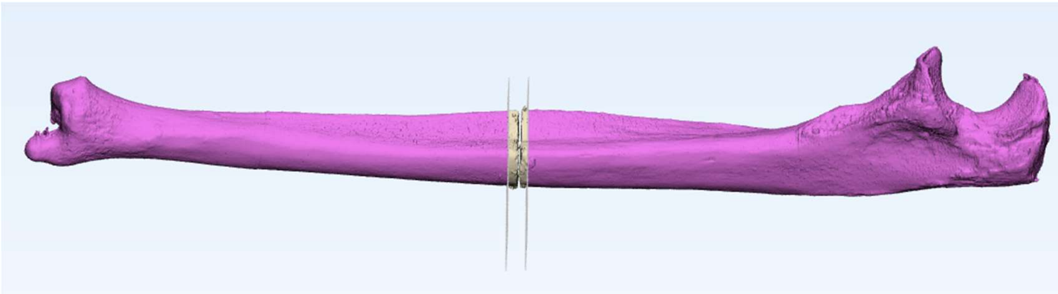

Figure 13: Selecting the ROI (purple) on a microCT ulna 3D model (bone color), with in the middle the physical cutting plane visible. The proximal and distal ROI are selected by inserting two cutting planes (grey) 2 mm from the physical cutting plane and deleting the 3D model between the cutting planes.

Study Parameters: mean volume distance +/- standard deviation (SD) [mm]

The distance mapping of the 3D model analysis resulted in a volume distance in millimeter (mm) between the sCT or CT and the microCT 3D model. For every analysis, the mean difference and its standard deviation (SD) were determined. A positive distance indicates a larger synthetic CT or CT 3D model compared with the microCT 3D model.

2.2.2 Saw guide analysis

To test whether (the found volume distance of) the sCT was sufficient accurate for 3D printing of saw guides, a saw guide analysis was conducted.

The first step was to design saw guides. The designs were based on currently clinical used lower arm osteotomy saw guides. Per radius or ulna bone, a proximal and distal saw guide was designed. For the clinical applicability, the location of the saw guides was chosen on the following criteria: cutting away a minimal soft tissue to reach the bone, exclusion of muscle inertia locations (Figure 2), and clinical accessible. [35] The chosen locations were discussed with an academic orthopedic surgeon before finalization. For the radius, the proximal saw guide was located anterior and the distal saw guide posterior (Figure 14). The proximal and distal ulna saw guides were placed both posterior (Figure 15).

To saw guides were generated with the sCT- and CT-based 3D bone models in 3-matic, based on the method by Caiti et al. [7] who also investigated two types of lower arm osteotomy saw guides. The saw guide basis was created by expanding the 3D bone model 2 mm outwards. With this, a hollow enlarged 3D model of 2 mm thickness was created. On the predetermined locations, 2 half cylinders with a length of 4 mm were cut-off from the enlarged 3D model by placing 4 perpendicular and 2 parallel cut-off planes. These half cylinders formed the base of the saw guides, see Figure 14. Per 3D bone model, the cutting planes were identical for all three 3D models from the CT-, sCT- and microCT scan.

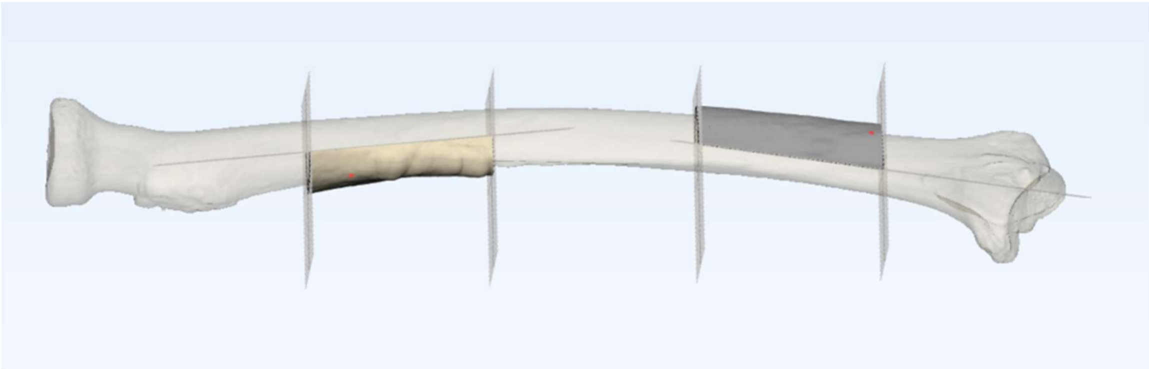

Figure 14: A radius CT-3D model with two half cylinders located proximal and distal on the bone, created with the 4 perpendicular and 2 parallel cut-off planes in 3-matic.

As reference point per saw guide design, a rectangle box (20 x 5 x 10 mm) was placed on the top of the saw guide base (Figure 15). The box's position was identical for the corresponding CT-, sCT- and microCT saw guide. For saw guide identification, the bone part location was placed on one side of the box (for example 'P1 Radius Proximal'). In addition, a randomized letter 'A' or 'B' was added to the sCT or CT saw guides and for the microCT the name 'microCT' was added. Per radius or ulna bone, six saw guides were designed: a proximal and distal CT-, sCT- and microCT-based saw guide. In total 96 saw guides were created, respectively 32 sCT, 32 CT and 32 microCT saw guides. The 64 sCT- and CT-based saw guides were 3D-printed from polyamide 12 (Oceanz, Ede, The Netherlands; print accuracy 0.12 mm in all directions).

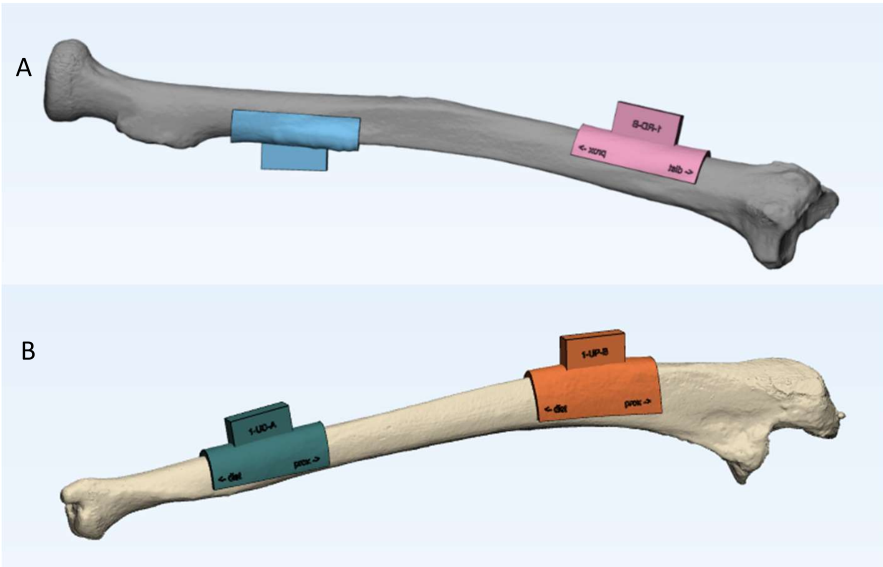

*Figure 15: **A)** A radius CT-3D model with its distal (pink) and proximal (blue) saw guide and **B)** A ulna CT-3D model with its distal (green) and proximal (orange) saw guides in 3-matic.*

With the 3D-printed saw guides, six blinded observers (two orthopedic surgeons, two orthopedic surgeons in training and two orthopedic researchers, with one of the researchers with the most extensive saw guide experience of all observers) executed the saw guide study. One observer conducted the saw guide study two times on separate days, to analyze the intra observer variability. All observers were asked to place the 64 randomized (sCT and CT) saw guides in two rounds (respectively round 'A' and round 'B') on the corresponding ulna or radius bone part. Figure 16 shows a 2D planning the observers used to find the correct position for the saw guide on the bone. This study used a 2D planning, instead of the clinically used 3D planning to save expenses, since a 3D planning includes a true sized 3D-printed bone with corresponding saw guide for every saw guide thus for this study in total 64 3D-prints.

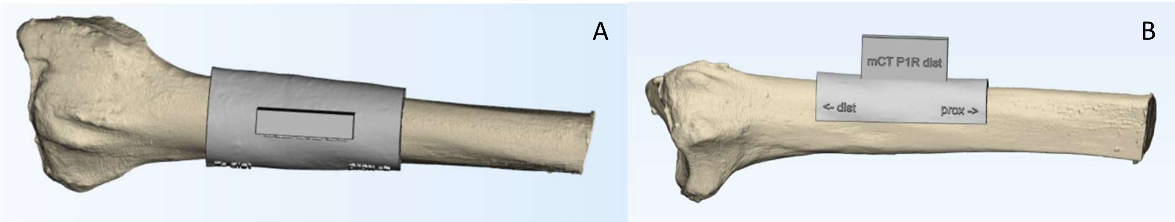

*Figure 16: 2D planning used by the observers during the saw guide study to find the correct position on the bone. This example of a distal radius saw guide with **A**) A posterior view and **B**) sagittal view.*

Grading of the saw guide fitting (subjective analysis)

Based on the 'fitting' of the saw guides on the corresponding bone part, the final location was chosen by the observers. The bone with corresponding saw guide were then fixated in a holder, see Figure 17A. After placement of a saw guide the observer was asked to grade (1-10) the 'fitting' satisfaction of the saw guide on the bone part as subjective analysis. The higher the grade, the better the fit was found by the observer.

Study parameter: grading of the saw guide 'fitting' per observer (1-10)

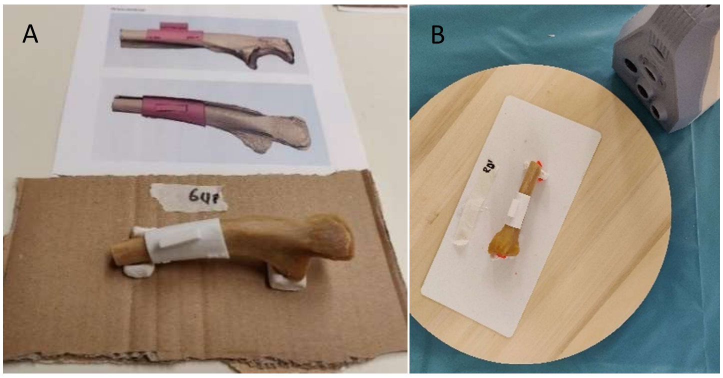

*Figure 17: **A**) Proximal ulna bone with placed saw guide in its holder (bottom) and 2D saw guide planning (top). **B**) The used spinning plateau for scanning with in the middle a distal radius bone and the optical 3D scanner on the right.*

Positioning accuracy saw guides (objective analysis)

As objective analysis, the positioning accuracy of the saw guides were measured. For this measurement an optical 3D scanner was used (Artec Space Spider, Artec 3D, Luxembourg, Luxembourg; 3D reconstruction resolution 0.1 mm) provided by 4C (Emmen, The Netherlands). Of every bone with placed saw guide, an optical 3D scan was generated with in total 64 optical 3D scans per observer. For the optical scan, the bone with saw guide in the bone part holder was placed the middle of a spinning plateau, see Figure 17B. The bone and saw guide were captured with the optical 3D scanner by manually holding the scanner at on average a distance of 20 cm from the bone, depended on the distance meter of the optical 3D scanner. This meter indicated the optimal range to hold the scanner based on the center of the depth of view. By rotating the plateau, the object was scanned with 8 frames per second and 'high sensitivity'-

setting the object. With the provided software Artec Studio (Artec 3D, Luxembourg, Luxembourg) 3D models were obtained from the optical scans. First on the raw optical scan the plateau was removed and then the 3D models were reconstructed with the following settings: 'fine registration', 'global registration', 'outlier removement', 'sharp fusion'. Second, three 3D models were generated from the raw optical 3D scan: a 3D model of the bone part, the saw guide and the bone part with saw guide. Finally, after reconstruction the 3D models were exported as binary STL-file, see Figure 18.

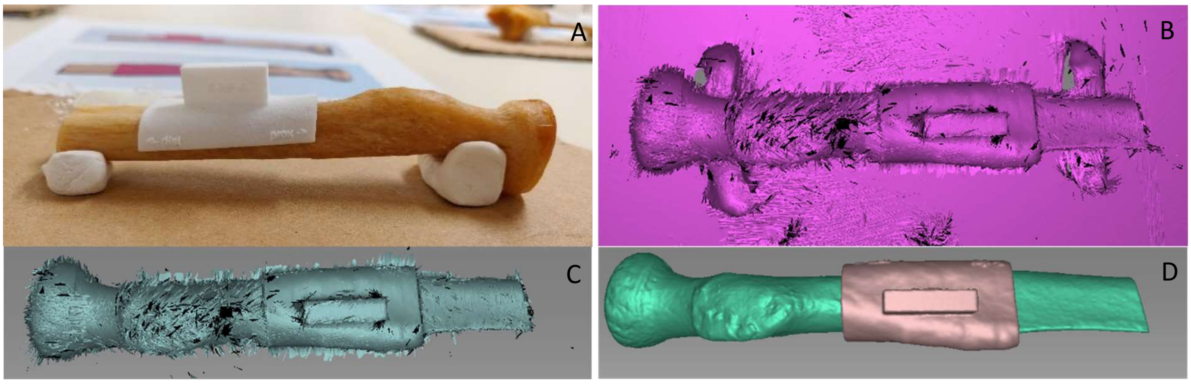

*Figure 18: **A**) A proximal radius with saw guide during the saw guide study. **B**) Raw image made by the optical scan. **C**) With processing steps in Artec Studio the base is removed. **D)** The final optical scan with green the bone and bronze the saw guide.*

Finally, the positioning accuracy was objectively analyzed based on the method of Caiti et al. [7]. This method was used, since this study also investigated the positioning accuracy of saw guides. The position accuracy was analyzed by calculating the displacement of the placed CT and sCT saw guides relative to the gold standard microCT saw guide planned position. This was executed by calculating the transformation in MATLAB, containing the translation and rotation of the placed saw guides.

For this, bone parts on the optical 3D models were registered to their corresponding bone parts on the microCT 3D model with an ICP-algorithm in MATLAB, see Appendix A – ICP Algorithm. Figure 19 shows the optical 3D bone models (red and blue) after registration to the corresponding microCT 3D model (green).

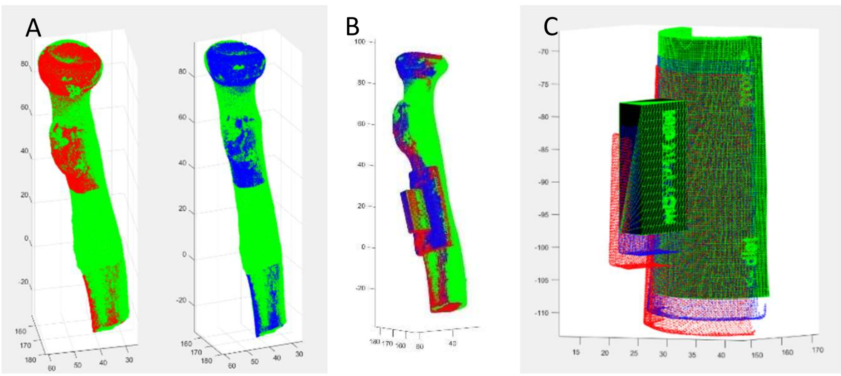

*Figure 19: **A**) The CT and sCT optical scan 3D models, red saw guide 'A' and blue saw guide 'B', with the corresponding microCT 3D model (green) after bone-bone registration. **B**) The 3D bone models after bone registration with their saw guides and **C**) the saw guides after bone registration, showing the displacements. On the axis, the length in mm is displayed.*

After the bone-bone registration, the translation and rotation between the reference boxes on the placed and planned saw guides were calculated. This transformation was calculated with two consecutive ICP-algorithms in MATLAB. For this, the optical scans reference box was selected on the 3D models (Figure 20A) and the microCT reference box was interpolated to obtain an equal amount of datapoints from both reference boxes. As final check, the optical 3D saw guide models were transformed with the calculated transformation and displayed with the microCT reference box (Figure 20B).

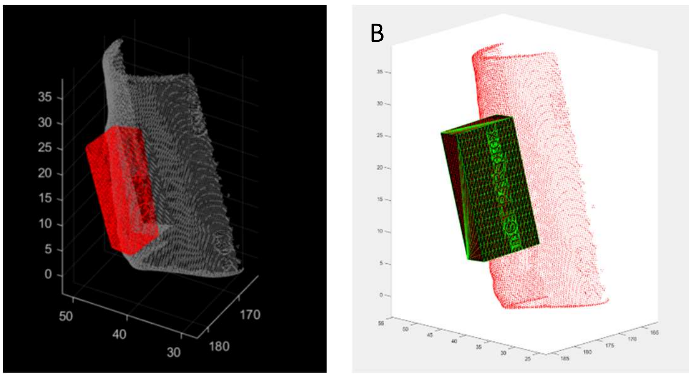

*Figure 20: **A**) The selected ROI of the box on the optical scan (red). **B**) The transformed optical saw guide (red) is displayed with the corresponding microCT box (green/black). On the axis, the length in mm is displayed.*

For the positioning accuracy of the CT and sCT saw guides, a translation (mm) and rotation (degrees) displacement are determined from the transformation matrix $\boldsymbol{T}$ calculated with the ICP-algorithm. This 4x4 transformation matrix $\boldsymbol{T}$ contains the 3x1 translation vector $\boldsymbol{Tr}$ and 3x3 rotation matrix $\boldsymbol{R}$:

$$\boldsymbol{T} = \begin{bmatrix} & [\boldsymbol{R}] & & \boldsymbol{Tr} \\ 0 & 0 & 0 & 1 \end{bmatrix} = \begin{bmatrix} \begin{bmatrix} r_{11} & r_{12} & r_{13} \\ r_{21} & r_{22} & r_{23} \\ r_{31} & r_{32} & r_{33} \end{bmatrix} & \begin{matrix} \Delta x \\ \Delta y \\ \Delta z \end{matrix} \\ \begin{matrix} 0 & 0 & 0 \end{matrix} & 1 \end{bmatrix}$$

In total, eight saw guide displacement translation and rotation errors for every saw guide and every observer were calculated. A larger value indicates a larger displacement, relative to the planning on the microCT. With the absence of maximum allowed displacement errors, this study compared the sCT saw guides displacement errors to the CT saw guides displacement errors to determine the position accuracy.

Translation displacement

Three displacement errors in the x-, y- and z-direction are derived from the translation vector $\boldsymbol{Tr}$ and defined as $\Delta x,\ \Delta y,\ \Delta z$ in mm. The direction of these saw guides can be seen in Figure 21.

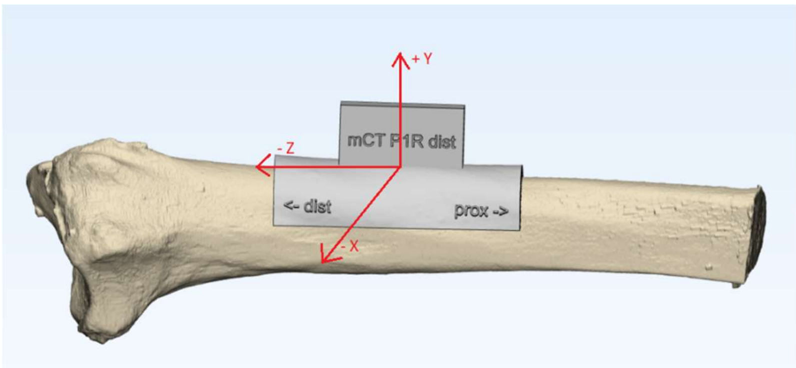

Figure 21: Directional vectors on the reference box of the saw guide. For every saw guide these directions were the same.

Rotation displacement

Three displacement errors around the x-, y- and z-axis are derived from the rotation matrix $\boldsymbol{R}$ and defined as φ_x, φ_y, φ_z in degrees. These rotation errors are calculated with yaw, pitch and roll [51]:

$$\begin{bmatrix} r_{11} & r_{12} & r_{13} \\ r_{21} & r_{22} & r_{23} \\ r_{31} & r_{32} & r_{33} \end{bmatrix} = \begin{bmatrix} \cos\alpha\cos\beta & \cos\alpha\sin\beta\sin\gamma - \sin\alpha\cos\gamma & \cos\alpha\sin\beta\cos\gamma + \sin\alpha\sin\gamma \\ \sin\alpha\cos\beta & \sin\alpha\sin\beta\sin\gamma + \cos\alpha\cos\gamma & \sin\alpha\sin\beta\cos\gamma - \cos\alpha\sin\gamma \\ -\sin\beta & \cos\beta\sin\gamma & \cos\beta\cos\gamma \end{bmatrix}$$

$$= \textit{Rotation matrix } \boldsymbol{R}(\alpha, \beta, \gamma) = \boldsymbol{R}(\phi_x, \phi_y, \phi_z)$$

- Yaw represents the rotation in the vertical axis, for the saw guides the z-rotation (φ_z). To calculate the rotation error in the z-direction:

$$\phi_z = \tan^{-1}\left(\frac{r_{21}}{r_{11}}\right) * \frac{180}{\pi} \quad (degrees)$$

- Pitch represents the rotation in the transverse axis, for the saw guides the y-rotation (φ_y). To calculate the rotation error in the y-direction:

$$\phi_y = \tan^{-1}\left(\frac{r_{32}}{r_{22}}\right) * \frac{180}{\pi} \quad (degrees)$$

- Roll represents the rotation in the longitudinal axis, for the saw guide the x-rotation (φ_x). To calculate the rotation error in the x-direction:

$$\phi_x = \sin^{-1}(r_{31}) * \frac{180}{\pi} \quad (degrees)$$

Total translation ΔT and total rotation error ΔR

Besides the six DOF, a total translation error ΔT (mm) and total rotational error ΔR (degrees) were calculated based on [21]:

$$\Delta T = \sqrt{(\Delta x)^2 + (\Delta y)^2 + (\Delta z)^2} \quad (mm)$$

$$\Delta R = \sqrt{(\varphi_x)^2 + (\varphi_y)^2 + (\varphi_z)^2} \quad (degrees)$$

Study parameters: mean translation [mm] and rotation [degrees] error in six DOF +/- SD

Total rotation [mm] and total rotation [degrees] error +/- SD

2.3 ICP algorithm

To register 3D-models efficiently and accurately, an ICP-algorithm was used. [20] For this, the 3D models were converted to point clouds: a model in a 3D space with an X-, Y- and Z-coordinate. An ICP-algorithm finds the closest point on one of the source point clouds (CT or sCT) to a given reference point on the other point cloud (microCT). For these points, the local minimum of a mean square distance metric is calculated. This calculation is repeated for all points on the source point cloud to the reference point cloud. With the mean square distances, a translation and rotation matrix are determined to minimize the error metric:

Input*:* a source and reference *point cloud*, criteria for stopping and executing iterations (number of iterations, matching method 'kDtree algorithm' [52], minimization method 'point to point')

Output*:* 4x4 transformation matrix ***T,*** including 3x3 rotation matrix ***R*** and 3x1 translation vector ***Tr***

For each point (X, Y, Z) in the source point cloud

- Compute the closest point in the reference point cloud
- Estimate the rotation and translation by calculating the root mean square point to point distance metric, to register each source point to its match found in the previous step. For this, the worst 50

percent point pairs are rejected based on their Euclidean distance as weighting factor. The rotation matrix and translation vector are combined in a transformation matrix.

- Transform the source points using the obtained transformation matrix.
- Iterate until done

End

Show the transformed point cloud with the reference point cloud

2.4 Statistical analysis

The study parameters were statistical analyzed using SPSS v. 25 (IBM Corp, Armonk, NY, USA). In total 448 data points (7 operators x 8 lower arms x 4 halve bones x 2 guide designs) were analyzed.

To test the intra- and interobserver grading agreement of the observers, a Cohen's kappa test was applied on these ordinal paired data where the κ represents the agreement value: κ < 0 reflects 'poor', κ = 0-0.2 reflects 'slight', κ = 0.21-0.4 'fair', κ = 0.41-0.6 'moderate', κ = 0.61-0.8 'substantial' and κ > 0.81 'almost perfect' agreement. [53]

With the calculated translation and rotation errors, continuous distributed data was generated. The question was raised: 'What kind of test do we need, what does this tell us and what is the clinical relevance? Therefore, the proper statistical tests were applied on the data:

1) A one sample two-tailed t-test investigated whether the mean translation and mean rotation displacements of the CT saw guides are equal to the mean displacements from the sCT saw guides or differ significantly. A p-value < 0.025 was considered significant for this test, since it tests the mean from both sides and not testing the relation in one direction like a one-tailed t-test.
2) Bland-Altman plots of the ΔT and ΔR were created to check whether the new method (the sCT-based saw guides) agrees sufficiently well with the 'old' method (the CT-based saw guides). With the maximum allowed displacements values unknown, this indirect method was used. For the Bland-Altman plots, two types of limits of agreement (LoA) were calculated and displayed: $1.96 \times SD$ of the intra- and inter-observer variability, with the inter-observer variability as the maximum difference. If 95% of the data of the ΔT and ΔR lies within the calculated LoA, the displacement errors of the CT- and sCT-based saw guides can be seen as equivalent.
   a. The inter-observer variability was defined as the maximum displacement difference found for the 'old' method; the CT saw guides. For every CT saw guide, the minimum and maximum found values were used to calculate the maximum translation and rotation differences. From all maximum rotation and translation displacement differences, a SD was determined. These two SD's were used to calculate the $1.96 \times SD$ as LoA.
   b. The intra-observer variability was defined as the translation and rotation displacement difference for the CT saw guides. The two SD of these differences were used to calculate the $1.96 \times SD$ as LoA. For this one observer executed the saw guide study two times.
3) Based on the method from Caiti et al. [7], Box plots were created to analyze the differences between saw guide locations.

3. Results

3.1 3D model validation

Bone surface differences between the 3D models from the CT, sCT and microCT were quantified with a distance analysis. The results can be seen in Table 1 and Figure 22. The positive values in Table 1 indicate that the sCT- and CT-based 3D models are overall larger than the microCT-based 3D model. When analyzing differences between the CT- and sCT-based 3D models, outlier errors are frequently seen at the most proximal and distal end of the bones (Figure 22, blue). One sCT-based 3D model included a calcified vessel or tendon due to similar generated HU values to bone, see Figure 23.

Table 1: Distance mapping of the sCT and CT 3D model surfaces to the microCT 3D model in 3-matic. A positive value indicates that the sCT or CT model larger than the microCT model is.

	Signed error: Mean (SD) [mm]	RMS error [mm]
CT	0.236 (0.119)	0.267
sCT	0.265 (0.303)	0.408

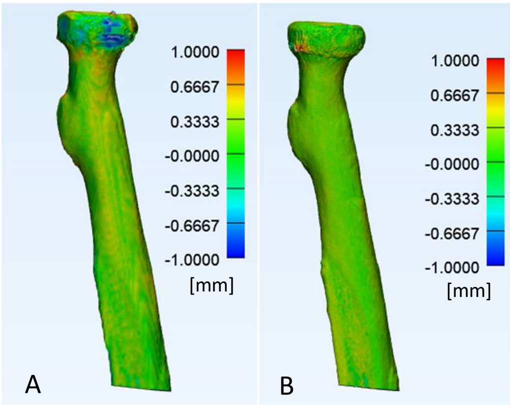

*Figure 22: Distance mapping of a proximal radius 3D model with **A**) sCT vs. microCT and **B**) CT vs. microCT. The color bar indicates differences (mm) between the microCT and the sCT or CT within a -1 and 1 mm range. A positive value indicates a larger sCT or CT model than the microCT model. Proximal the largest errors are seen.*

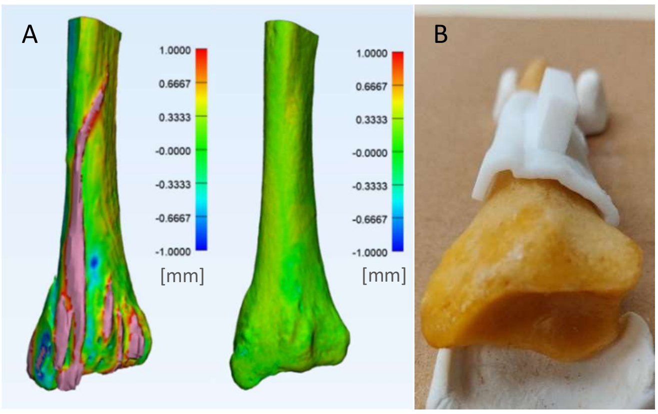

*Figure 23: **A**) Distance mapping of a distal radius 3D model: Left sCT vs. microCT, right CT vs. microCT. The color bar indicates differences (mm) between the microCT and the sCT or CT within a -1 and 1 mm range. A positive value indicates a larger sCT or CT model than the microCT model. The left sCT-based model shows an outlier in red. **B**) The corresponding saw guide of the distal radius based on the sCT, showing a gap that is not seen on the bone.*

3.2 Saw guide analysis

3.2.1 3D-printed saw guides

Rendered examples of the 3D-printed CT- and sCT-based saw guides can be seen in Figure 24. In general, the guides look identical, only a close-up the inside of CT-based saw guides shows 'waves' (Figure 24B).

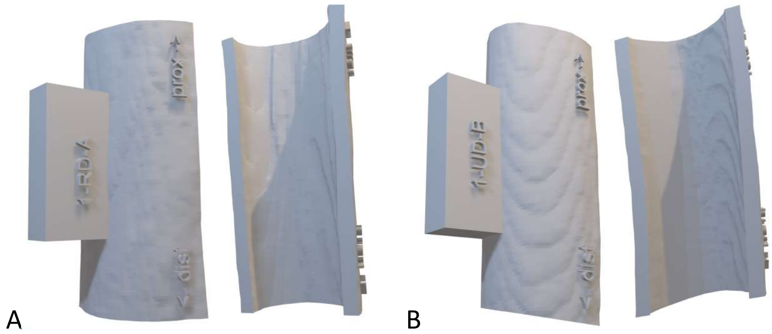

*Figure 24: Corresponding 3D-printed distal radius saw guides with **A**) The sCT and **B**) the CT saw guide.*

3.2.2 Bone shrinkage analysis

A second microCT (reconstructed resolution of 0.05 mm) was obtained of eight half bones (two radius and two ulna bones) after the saw guide study to analyze influences of processing steps: cutting soft tissue, simmering and dehydration over time. With a distance analysis, an average volume difference between the pre- and poststudy microCT of -0.043 +/- 0.124 mm (mean +/- SD) was found (Table 2). A negative value indicates that the bone after the saw guide study are smaller in volume than the corresponding bone before the saw guide study. Furthermore, a reconstruction malalignment smaller than 0.05 mm was visible in the center of the bones when comparing the pre- and post-study microCT's, see Figure 25.

Table 2: Distance mapping of the microCT 3D model surface of eight halve bones before and after the saw guide study. Bone part 1 and 2, 3 and 4, 5 and 6 and 7 and 8 are from the same specimen.

Bone part	**1**	**2**	**3**	**4**	**5**	**6**	**7**	**8**	**Average**
Mean [mm]	-0.037	-0.047	-0.036	-0.037	-0.028	-0.031	-0.065	-0.061	-0.043
SD [mm]	0.060	0.130	0.142	0.111	0.044	0.261	0.117	0.124	0.124

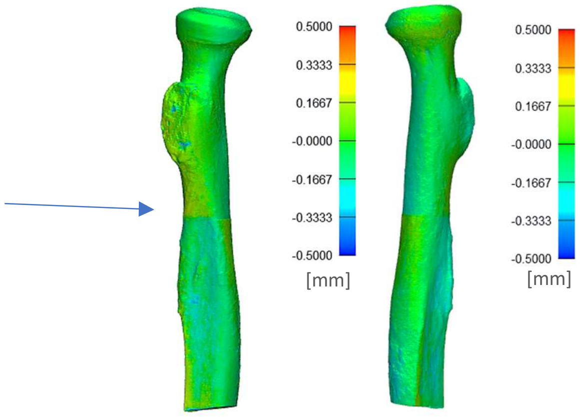

Figure 25: Distance mapping between the pre- and poststudy microCT 3D model of a proximal radius of P1. The red indicates a positive distance value (volume increase) and blue a negative distance value (volume decrease) in the -0.5 to 0.5 mm range. In the middle of both illustrated bones a small reconstruction line is visible (arrow).

3.2.3 Main study parameter results

Subjective analysis

The average grade for the fitting satisfaction of the CT-based saw guides on the bones was 6.9 (SD: 0.9) and for sCT-based 6.3 (SD: 1.3), see Figure 26. When distinguishing between saw guide location, the average grade for proximal and distal radius saw guides were 7.1 (SD: 1.5) and 6.5 (SD: 1.7) and for proximal and distal ulna saw guides were 6.9 (SD: 1.5) and 5.8 (SD: 2.2). Furthermore, the inter- and intra-observer variability for all saw guide grades was respectively 'slight' (κ = 0.154) and 'moderate' (κ =0.442) agreement (Appendix B – Statistics SPSS).

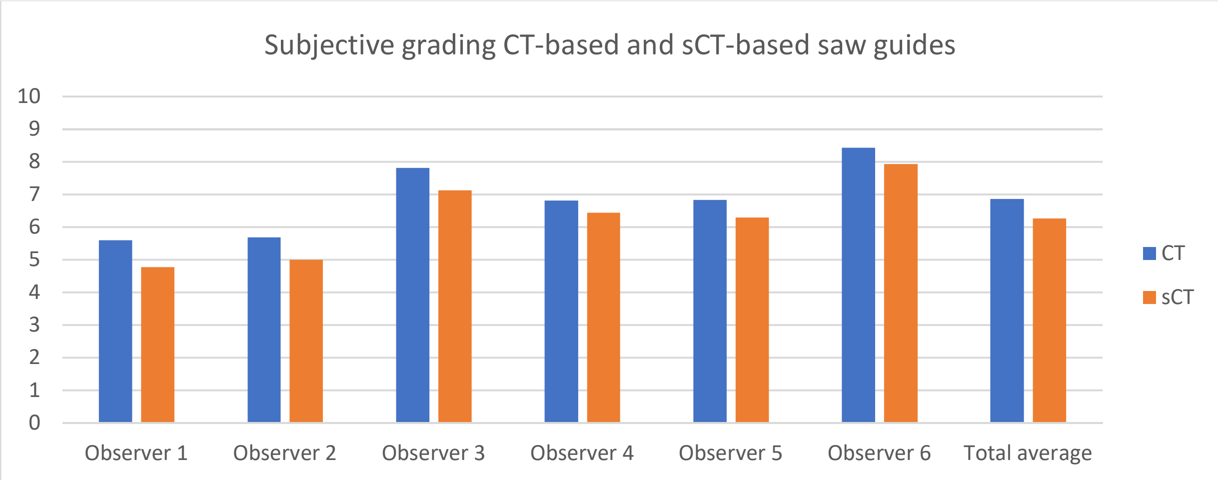

Figure 26: Average subjective grading score per observer and in total. In blue the grading of the CT- and in orange the sCT-based saw guides are displayed. Observer 1 and 4 are orthopedic surgeons, observes 5 and 6 are orthopedic surgeons in training and observer 2 and 3 are orthopedic researchers.

Objective analysis

Table 3 shows the average translation (Δx, Δy, Δz, ΔT) and rotation (φx, φy, φz, ΔR) errors of the CT- and sCT-based saw guides. The largest errors are seen in the z-direction or around the z-axis (Figure 21). To test if the CT- and sCT-based saw guide errors differed significantly, a one sample t-test ($p < 0.025$ significant) provided a p-value of 0.284 for ΔT and 0.216 for ΔR.

Table 3: Average (+/- SD) translation and rotation errors of the CT- and sCT-based saw guides placed by the six observers.

Saw guide	Translation: mm (+/- SD)					Rotation: degrees (+/- SD)				
	Δx	Δy	Δz	ΔT average	ΔT max diff	φx	φy	φz	ΔR average	ΔR max diff
CT-based	-0.04 (0.65)	-0.10 (0.29)	-0.50 (1.48)	2.44 (1.41)	4.46 (3.43)	-0.06 (0.48)	0.04 (0.52)	-0.68 (2.70)	3.76 (3.31)	6.92 (6.82)
sCT-based	0.00 (1.35)	-0.15 (0.59)	-0.65 (1.90)	2.82 (1.60)	4.50 (2.83)	0.10 (0.71)	0.20 (0.67)	-2.14 (6.10)	4.89 (4.87)	6.99 (6.81)

A Bland-Altman plot that compares the means of the average CT and sCT-based saw guide ΔT and ΔR is displayed in Figure 27 and Figure 28 with the LoA $1.96 \times SD$ of the intra- and inter-observer variability. For both the translation and rotation variability, the values fall between the inter-observer variability LoA.

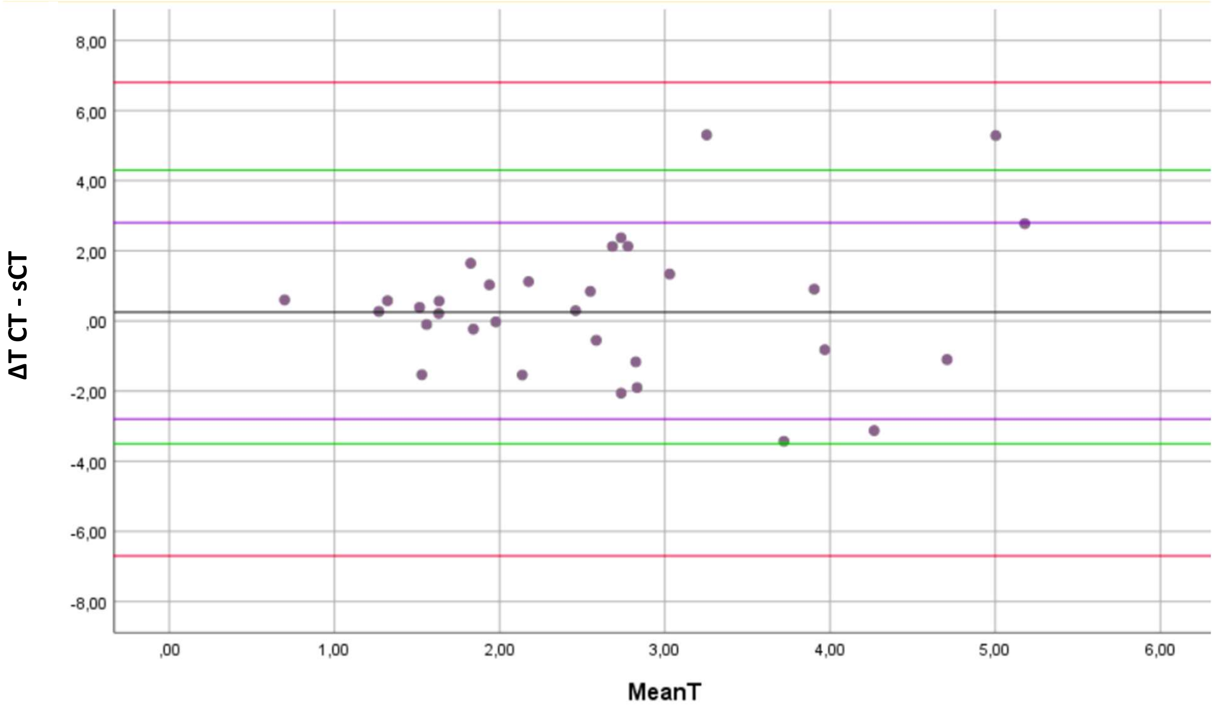

Figure 27: Bland-Altman plot of the total translation error ΔT difference between CT- and sCT-based saw guides with a mean line (grey, 0.38 mm) and a 95% confidence interval of LoA 1.96 x SD (green). The purple and red lines are respectively the intra- and interobserver variability LoA (1.9 x SD).

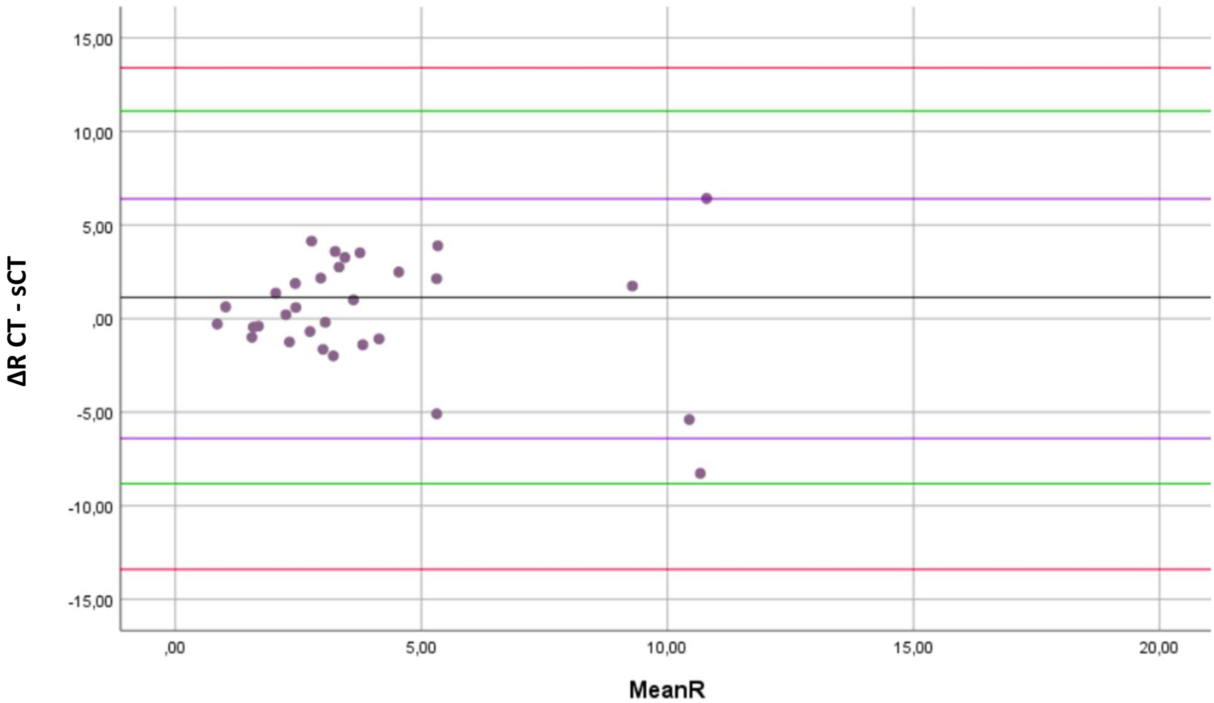

Figure 28: Bland-Altman plot of the total rotation error ΔR difference found between CT- and sCT-based saw guides with a mean line (grey, 1.13 degrees) and a 95% confidence interval of LoA 1.96 x SD (green). The purple and red lines are respectivley the intra- and interobserver variability LoA (1.96 x SD).

Displacements results per saw guide location for the CT- and sCT- based saw guides are displayed in the boxplots in Figure 29, with A and B the average ΔT and ΔR. For both guide designs, distally the translation displacement and proximally the rotation displacement are the lowest. Figure 29C and D show the translation (Δx, Δy, Δz) and E and F the rotation errors (φx, φy, φz) of the proximal and distal saw guides. The translation and rotation displacements are the largest in the z-direction for both saw guide designs.

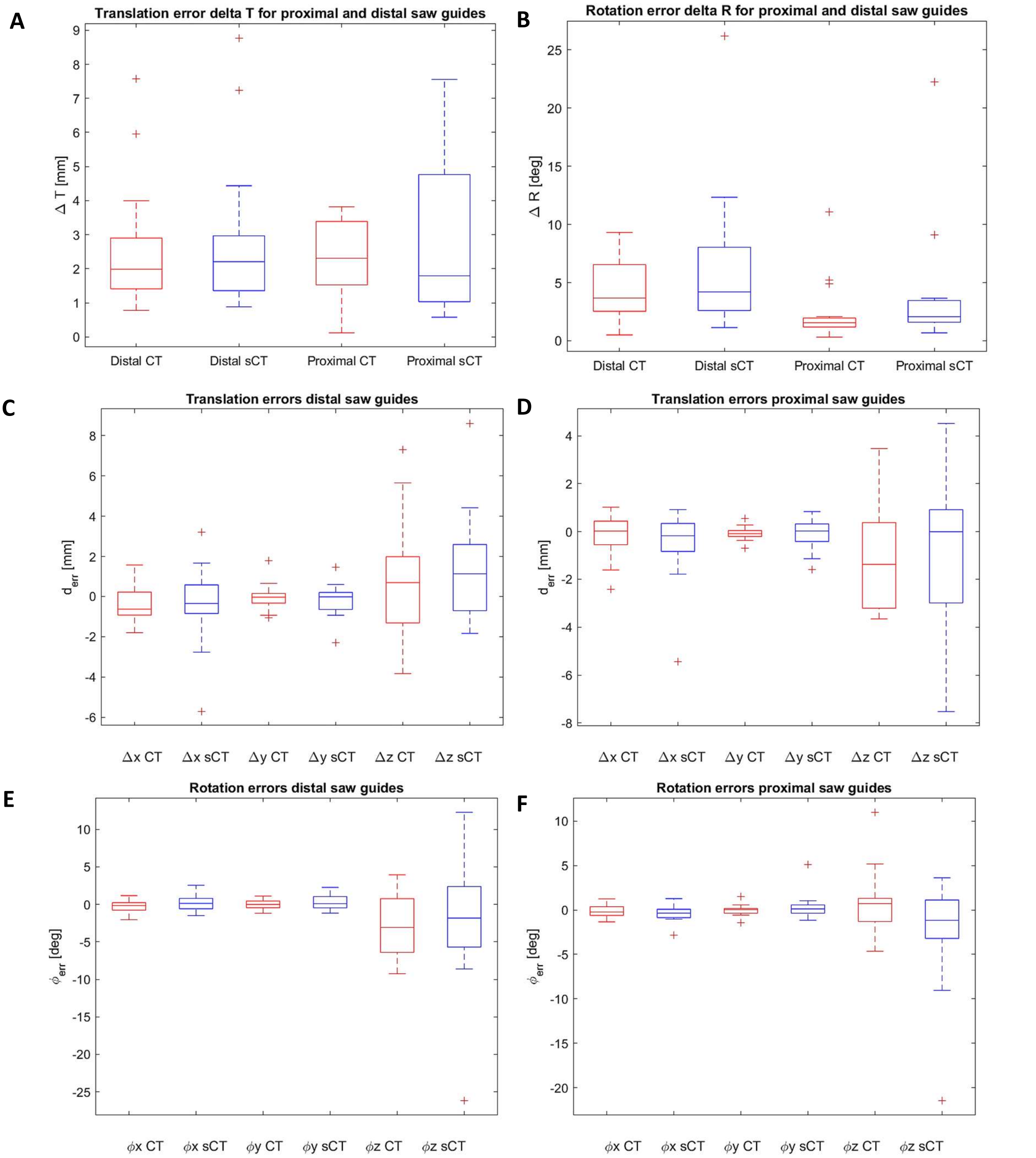

*Figure 29: Box plots of **A)** total translation error ΔT, **B)** total translation error ΔR, **C)** translation errors of distal guides, **D)** translation errors proximal guides, **E)** rotational errors distal guides and **F)** rotational errors proximal guides with CT- (red) and sCT-based (blue) guide types. The central mark in the box indicates the mean, the top (Q3) and bottom (Q1) box edges are the 25th and 75th percentile. The whiskers extend to the most extreme data and outliers are displayed in red '*'.*

To analyze expertise influence, the ΔT and ΔR for all observers are shown in Table 4 and Figure 30. Observer 1 and 4 are orthopedic surgeons, observes 5 and 6 are orthopedic surgeons in training and observer 2 and 3 are orthopedic researchers, where observer 3 has extensive saw guide experience. For this study, the average execution time was 69 minutes (SD: +/- 30 min), with as longest time 120 minutes (observer 3) and shortest 40 minutes (observer 6). Observer 3 shows the lowest displacement errors.

Furthermore, in total 8 percent (59/768; 64 saw guides x 6 observers x 2 errors) saw guides error outliers were seen (see asterisk (*) in Figure 30). Of these outliers, 81 percent (48/59) are ulna saw guides and 73 percent (43/59) are distal located ulna saw guides. An example of a distally located ulna saw guide placed on the corresponding bone that was reported as outlier can be seen in Figure 31.

Table 4: Average errors ΔT and ΔR (mean +/- SD) of CT- and sCT-based saw guides found per observer.

	Observer 1	Observer 2	Observer 3	Observer 4	Observer 5	Observer 6
ΔT CT	3.93 (3.48)	1.82 (1.18)	1.15 (0.98)	2.44 (2.59)	2.86 (2.86)	2.45 (1.53)
ΔT sCT	3.82 (3.05)	2.09 (1.90)	1.82 (1.45)	3.40 (3.09)	2.95 (2.30)	2.84 (2.19)
ΔR CT	4.05 (6.93)	3.58 (3.93)	2.45 (2.74)	4.44 (6.14)	4.63 (4.48)	3.40 (2.84)
ΔR sCT	5.98 (6.83)	4.49 (6.23)	3.77 (4.02)	5.92 (5.64)	5.41 (6.98)	5.11 (5.90)

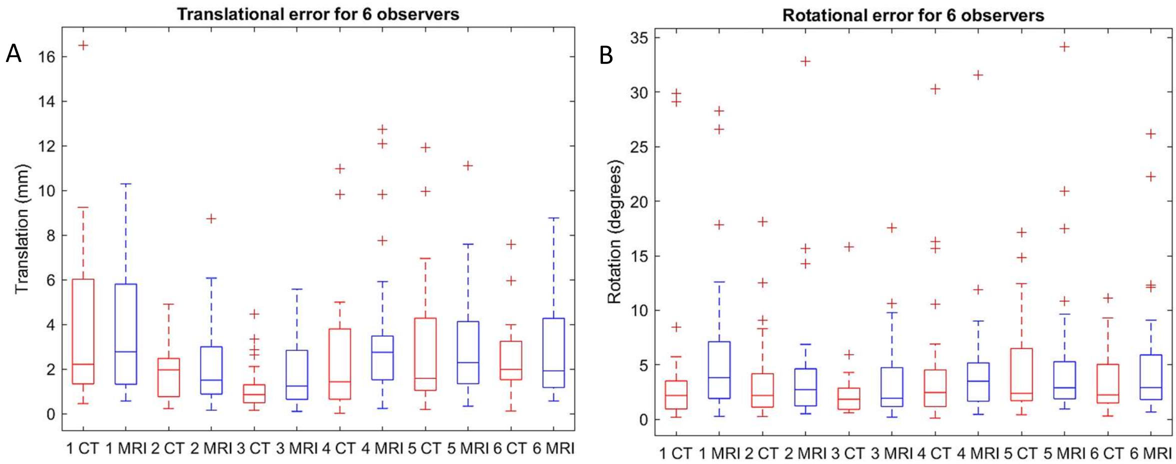

*Figure 30: Box plots of the **A)** total translation error ΔT and the **B)** total translation error ΔR, dependency on the six observers and on CT- (red) or sCT-based (blue) guide design.*

Figure 31: Distal placed ulna saw guide during saw guide study.

4. Discussion

With this study, we have investigated a new method to generate 3D-printed patient-specific saw guide for lower arm osteotomy without ionizing radiation based on a synthetic CT scan. This study aimed to assess the position accuracy of the sCT-based saw guides when compared to the currently used CT-based saw guides. For this purpose, these two saw guides types were analyzed on cadaveric radius and ulna bones.

With the absence of allowed values for the maximum displacement errors for ulna and radius saw guides, two statistical analyses were performed to evaluate if there are differences between the displacements of the CT- and sCT-based saw guides. First, the one sample two-tailed t-test ($p < 0.025$ significant) shows no significant difference between the total translation (p-value = 0.284) and total rotation (p-value = 0.216) displacement of the CT- and sCT-based saw guides. Second, all data points on the Bland-Altman plots of the total rotation and total translation errors (Figure 27 and Figure 28) lie between the LoA of the inter-observer variability. This implies that, despite initial resolution differences, displacement differences of the CT- and sCT-based saw guides are equivalent.

When comparing the results of this study to comparable publications, some noteworthy differences are found. Caiti et al. [7] analyzed positioning errors of distal, mid-shaft and proximal radius saw guides. They showed that distal guides have the smallest total translation (ranged 0.25-1.8 mm) and total rotation (ranged 0.2-1.6 degrees) errors, when compared to proximal (respectively ranged 0.15-2.25 mm and 0.3-5.7 degrees) or mid-shaft guides (respectively ranged 0.4-3.2 mm and 1.3-7.3 degrees). These values are overall lower than the found positioning errors of this study (Figure 29) and in this study the smallest rotation errors are seen proximally (Figure 29B). These differences can be explained with several aspects. First of all, Caiti et al. used 3D-printed saw guides on 3D-printed radius bones from healthy subjects, while this study used real cadaveric radius and ulna bones to mimic clinical practice. The 3D print accuracy (0.17 mm versus 0.12 mm) and scan resolution (slice thickness 0.67 mm versus 0.8 mm and voxel size both 0.3 mm) were similar. However, the use of cadaveric bones could have resulted in larger position deviations than with 3D-printed bones. Secondly, different anatomical locations were used. Caiti et al. investigated three locations (distal, proximal and mid-shaft) on only radius bones, while this study focused on two locations (distal and proximal) for both radius and ulna bones. In addition, the saw guide designs of this study were created for malunions of lower arm fractures that cause pro- and supination disability resulting in more mid-shaft locations than the distal and proximal guides from Caiti et al. Thirdly, different saw guide lengths were used. The clinically based designs of this study had a length of 4 cm, while the Caiti et al. guides were minimal 5 cm (based on 20 percent of the bone length). With distally a wider radius bone and a longer guide length, the saw guide would have more anchors to hang on to, hence the higher accuracy.

Still, a found similarity between the results of Caiti et al. [7] and this study are that the largest translation and rotation errors are in the z-direction (Figure 29C-F); along the bone part length(Figure 21). In the z-direction, the saw guides have the most freedom of movement. When positioning, the saw guide mostly moves along this direction until a ‘fit’ on the bone is found causing the largest errors in this direction.

Two LoAs in Bland-Altman plots were used to analyze if the sCT saw guides agree sufficiently with the currently used CT saw guides: the intra- and inter-observer variability (Figure 27 and Figure 28). With all data points between the inter-observer variability LoA, the figures indicate that the sCT and CT saw guides agree sufficiently. However, the intra-observer variability LoA based on observer 3 does not include 95% of the data points. With the most extensive saw guide experience and the longest execution time (120 min versus 40 min; average 69 min) observer 3 generated the smallest displacement errors (Figure 30). Therefore, the intra-observer variability LoA may be strict to use as LoA.

The shrinkage analysis to analyze the processing step influences on the cadaver bones showed an average shrinkage of 0.043 mm, with a range of 0.028-0.065 mm (Table 2). Two halve bones of the same specimen showed a shrinkage larger than the 0.05 mm microCT resolution, respectively 0.065 mm and 0.061 mm. The overall physical shrinkage was less than the 0.5 mm found in literature. [22] Therefore, we can state that this shrinkage had minimal to no influence on the saw guide placement.

The negative distal translation displacement in the z-direction, can be explained with the positive values from the distance mapping in Table 1. This indicates that the CT and sCT 3D models are larger than the corresponding microCT 3D model. With the microCT as gold standard for the bone surface, the currently used CT overestimates the bone volume, which is also found in literature [54]. In practice this may be helpful to fit the guides over the periosteum and other interposed soft tissue, but this study used bones with only periosteum. Therefore, the 'oversized' saw guides were placed more towards the ends of the bones where the bones are wider and have more anchors.

There are several study limitations and recommendations that should be noted. First, the initial resolution of the CT-scan was higher than the MRI-scan, on which the sCT was based: 0.3 versus 0.7 pixel spacing, 0.8 versus 1.2 slice thickness and 0.4 versus 0.6 spacing between slices. This could have negatively influenced the accuracy of the sCT guides in comparison to the CT guides.

Secondly, the calculated displacement errors do not indicate how good or bad the clinical outcome of a lower arm osteotomy would be. The results show displacement errors in six DOF and a larger displacement indicates a less accurate cutting plane compared to the planning. Still, it is unknown which value ranges are acceptable and if certain directions are more important for the clinical outcome. Ma et al. [23] showed the clinical relevance of distal radius osteotomy guides by translating these displacement errors to correction errors of the ulnar variance, radial inclination and volar tilt. Especially ulnar variance, the relative length of the distal radius and ulna surfaces, seems to influence the clinical outcome [55]; errors of 3 mm or more are associated with a poor outcome due to radial shortening. [56] For this we assume that when looking at the orientation, Δz seems to have the most influence on ulnar variance and thus on the clinical outcome. When analyzing the results, no large differences between the saw guide designs are found: CT guides have 42 (Mean:-0.5, SD: 3.0, ranged -14.1 to 9.8) and sCT guides have 47 (Mean: -0.6, SD: 3.2, ranged -12.7 to 8.6) Δz-displacements larger than 3 mm (positive or negative) of the 192 measurements. A recommendation for future research is to compare the results from this study to those of Ma et al. by creating a virtual lower arm osteotomy model with the generated 3D models and apply the calculated displacement errors to determine the ulnar variance, radial inclination and volar tilt.

To provide more comparable results between observers in a clinical setting, it is recommended to set a time limit to execute the saw guide study. This could be based on the average clinically used time and provide a usable intra-observer LoA.

Furthermore, a recommendation to improve the clinical relevance would be to compare a clinically made CT-scans with the sCT-scan. The used CT-scan in this study was not made according to the clinical CT-scan protocol for a lower arm. The slice thickness and kVp are comparable, but a higher exposure mAs was used. This resulted in a CT-scan with a higher exposure, less noise and a better contrast compared to a clinical lower arm CT-scan. However, this did not influence differences between the CT and sCT, since the sCT-scan was trained using this ‘improved’ CT-scan. An option to test the resolution differences and its consequences of different CT-scans would be to generate two CT-scans of a cadaver lower arm: one made with the clinical protocol for lower arms and one with the settings used in this study.

Another limitation is the semi-automatic segmentation for the 3D models. Manual adjustments may have introduced errors in the 3D models, thus in the saw guides and eventually the saw guide fitting. A recommendation would be to investigate a fully automatic segmentation.

A limitation of the currently used sCT were the false positive structures and errors in their 3D models, due to inhomogeneous density near the radioulnar joints and soft tissue visualized as bone. Previous research [16] showed that false positive tendons occur on a sCT when structures are adjacent to bone and difficult to distinguish on the MR, causing the algorithm to interpreted the structures as bone. Besides false positive structures, sCT errors can be explained with magnetic field inhomogeneities in and different field of views per scan. When the neural network is trained with different field of views, the network has the least information about the border visualization. [16] Therefore, most errors are seen at the radioulnar joints, the distal or proximal bone ends (Figure 22). This sCT limitation could explain the difference in the average grading on the saw guide fitting by the observers (respectively a 6.9 versus a 6.3). In addition, Figure 23A shows a tendon as false positive bone on the sCT-scan and the corresponding saw guide’s ‘tendon’s location’ shows a gap (Figure 23B). Due to this gap, the sCT saw guide had a lesser fitting compared to the corresponding CT saw guide without a gap: an average sCT grading of 4.5 compared to an average 7.5 for the corresponding CT saw guide. This lesser fitting was also seen in a larger total translation error (2.8 mm versus 1.0 mm). The total rotation error (4.0 versus 5.7 degrees) showed no influence of the gap, likely due to the many anchors on the distal radius bone. Future research should use an updated version of the sCT-algorithm to overcome false positive structures and errors in the sCT. If the false positive structures or errors would still be present, another recommendation would be to correct for this during the 3D model segmentation when it would only require a minimal adaptation.

Using a clear grading definition and a smaller scale, for example from 1 to 5, would be another recommendation to get more consensus between observers. In this study no explicit definition was given to the observers to the grade fitting of the saw guides (1-10). This resulted in a low fitting satisfaction agreement for the intra- and inter-observer variability.

The observers may have been biased by seeing the grade of the corresponding saw guide in the previous round. Although the saw guides designs were randomized and the observers did not know which was CT- or sCT-based, the observers may have compared the designs instead of giving an objective grading to the current fitting. A recommendation would be to randomize the saw guide sequence to overcome this.

Moreover, the 3D-printed saw guides were not fixated during the saw guide study which could have resulted in supplementary errors. In clinical practice, a saw guide is fixated with k-wires [33]. This method was not used, since this resulted in drilling holes in the cadaveric bones, making the study not repeatable. In addition, glue as fixation used by Caiti et al. [7] was also not possible in this study, since the observer needed to place two saw guides on the saw bone during two rounds in a row and would be to time-consuming to remove. In the future, the design of the saw guide should be adjusted to create a more ‘click-fit’ design, creating fixation without extra material, to minimize supplementary errors.

Furthermore, patients treated with lower arm osteotomy have generally more deformed bones than the used cadaver bones. This results in a ‘natural’ fixation of saw guides on the bone. In addition, the patient’s bones are more curved and surrounded by muscles, ligaments and periosteum creating anchor locations for the saw guide. [3] The cadaver bones had less anchors, which could have induced saw guides position errors. This was visible when comparing saw guides locations. The lowest grades (average 5.8) and largest errors are seen at the distal ulna (Figure 31). The ulna is mostly round and has none to minimal anchors. A recommendation is to use 3D-printed bones from patients who are treated with lower arm osteotomy for a more realistic result.

For future use, if the sCT is proven equivalent to CT, the sCT-scan could be validated with a sCT-based saw guide patient study. An important aspect to analyze is the cost-effectiveness of this method. Although MRI does not use any radiation, MRI is costly and time-consuming. A lower arm MRI-scan required 30-60 minutes, while a CT-scan requires 15 minutes. [24, 25] Furthermore, the sCT could be validated to design and 3D-print other patient-specific saw guides and implants.

5. Conclusion

This study investigated a new approach to design 3D-printed patient-specific saw guides based on MR-imaged sCT without ionizing radiation. This was done with a saw guide study, which showed that displacement errors of CT- and sCT-based saw guides are equivalent to each other. However, only a slight agreement between observers was found when comparing the satisfaction of the fit of the CT- and sCT-based saw guides. Moreover, the found results need to be translated to patient outcomes to evaluate the clinical impact of the two saw guide designs. In addition, recommendations such as using an improved sCT algorithm and placing the saw guides on clinically comparable osteotomy bones in a future study should be investigated. When the currently found limitations of the sCT can be resolved, the sCT could be sufficient accurate to use in the clinic. Then the radiation free sCT could not only be used for lower arm osteotomy saw guides for children, but also for adults and other orthopedic patient-specific guides or implants.

References

1. Willemsen, K., et al., *Challenges in the design and regulatory approval of 3D-printed surgical implants: a two-case series.* The Lancet Digital Health, 2019. **1**(4): p. e163-e171.
2. Mulford, J.S., S. Babazadeh, and N. Mackay, *Three-dimensional printing in orthopaedic surgery: review of current and future applications.* ANZ journal of surgery, 2016. **86**(9): p. 648-653.
3. Dobbe, J.G., et al., *Computer-assisted planning and navigation for corrective distal radius osteotomy, based on pre-and intraoperative imaging.* IEEE Transactions on Biomedical Engineering, 2010. **58**(1): p. 182-190.
4. Martelli, N., et al., *Advantages and disadvantages of 3-dimensional printing in surgery: a systematic review.* Surgery, 2016. **159**(6): p. 1485-1500.
5. de Muinck Keizer, R., et al., *Three-dimensional virtual planning of corrective osteotomies of distal radius malunions: a systematic review and meta-analysis.* Strategies in Trauma and Limb Reconstruction, 2017. **12**(2): p. 77-89.
6. Vittas, D., E. Larsen, and S. Torp-Pedersen, *Angular remodeling of midshaft forearm fractures in children.* Clinical orthopaedics and related research, 1991(265): p. 261-264.
7. Caiti, G., et al., *Positioning error of custom 3D-printed surgical guides for the radius: influence of fitting location and guide design.* International Journal of Computer Assisted Radiology and Surgery, 2018. **13**(4): p. 507-518.
8. Kunz, M., et al., *Image-guided distal radius osteotomy using patient-specific instrument guides.* The Journal of hand surgery, 2013. **38**(8): p. 1618-1624.
9. Dirix, P., K. Haustermans, and V. Vandecaveye, *The value of magnetic resonance imaging for radiotherapy planning.* Seminars in radiation oncology, 2014. **24**(3): p. 151-159.
10. ICRP, *Radiological Protection in Medicine.* ICRP Publication 105, 2007. **37**(6): p. 1-63.
11. De Gonzalez, A.B., et al., *Relationship between paediatric CT scans and subsequent risk of leukaemia and brain tumours: assessment of the impact of underlying conditions.* British journal of cancer, 2016. **114**(4): p. 388.
12. Pearce, M.S., et al., *Radiation exposure from CT scans in childhood and subsequent risk of leukaemia and brain tumours: a retrospective cohort study.* The Lancet, 2012. **380**(9840): p. 499-505.
13. Kwon, O.-R., et al., *The effect of femoral cutting guide design improvements for patient-specific instruments.* BioMed Research International, 2015. **2015**.
14. Eley, K.A., S.R. Watt-Smith, and S.J. Golding, *"Black Bone" MRI: a novel imaging technique for 3D printing.* Dentomaxillofacial Radiology, 2017. **46**(3): p. 20160407.
15. Florkow, M.C., et al., *The impact of MRI-CT registration errors on deep learning-based synthetic CT generation.* UMC Utrecht, Image Sciences Institue and Radiotheraphy Department, Utrecht, The Netherlands, 2018: p. 4.
16. Zijlstra, F., et al., *CT synthesis from MR images for orthopedic applications in the lower arm using a conditional generative adversarial network.* arXiv preprint arXiv:1901.08449, 2019.
17. Van den Broeck, J., et al., *Segmentation accuracy of long bones.* Medical engineering & physics, 2014. **36**(7): p. 949-953.
18. Otsu, N., *A threshold selection method from gray-level histograms.* IEEE transactions on systems, man, and cybernetics, 1979. **9**(1): p. 62-66.
19. Rovaris, K., et al., *Segmentation Methods for Micro CT Images: A Comparative Study Using Human Bone Samples.* Brazilian dental journal, 2018. **29**(2): p. 150-153.
20. Besl, P.J. and N.D. McKay. *Method for registration of 3-D shapes*. in *Sensor fusion IV: control paradigms and data structures*. 1992. International Society for Optics and Photonics.
21. Kuo, H.Y., et al. *3D object detection and pose estimation from depth image for robotic bin picking*. in *2014 IEEE international conference on automation science and engineering (CASE)*. 2014. IEEE.
22. Gelaude, F., J. Vander Sloten, and B. Lauwers, *Accuracy assessment of CT-based outer surface femur meshes.* Computer Aided Surgery, 2008. **13**(4): p. 188-199.
23. Ma, B., et al., *A laboratory comparison of computer navigation and individualized guides for distal radius osteotomy.* International journal of computer assisted radiology and surgery, 2014. **9**(4): p. 713-724.
24. Shaw, A.S. and A.K. Dixon, *Multidetector computed tomography*, in *Grainger & Allison's Diagnostic Radiology: A Textbook of Medical Imaging*, A. Adam and A.K. Dixon, Editors. 2008, Churchill Livingstone: New York, NY.
25. Wilkinson, I.D. and M.N.J. Paley, *Magnetic resonance imaging: basic principles*, in *Diagnostic Radiology: A Textbook of Medical Imaging*, R.C. Grainger, et al., Editors. 2008, Churchill Livingstone: New York, NY.
26. Chia, H.N. and B.M. Wu, *Recent advances in 3D printing of biomaterials.* Journal of biological engineering, 2015. **9**(1): p. 4.
27. Menon, M., J. Walker, and C. Court-Brown, *The epidemiology of fractures in adolescents with reference to social deprivation.* The Journal of bone and joint surgery. British volume, 2008. **90**(11): p. 1482-1486.
28. Landin, L.A., *Fracture Patterns in Children: Analysis of 8,682 Fractures with Special Reference to Incidence, Etiology and Secular Changes in a Swedish Urban Population 1950–1979.* Acta Orthopaedica Scandinavica, 1983. **54**(sup202): p. 3-109.

29. Fuller, D. and C. McCullough, *Malunited fractures of the forearm in children.* The Journal of bone and joint surgery. British volume, 1982. **64**(3): p. 364-367.
30. Price, C.T. and D.R. Knapp, *Osteotomy for malunited forearm shaft fractures in children.* Journal of Pediatric Orthopaedics, 2006. **26**(2): p. 193-196.
31. Trousdale, R. and R. Linscheid, *Operative treatment of malunited fractures of the forearm.* The Journal of bone and joint surgery. American volume, 1995. **77**(6): p. 894-902.
32. Surgeons, A.A.o.O., *Adult forearm fractures.* Orthoinfo, 2011. **Diseases & Conditions**.
33. Mader, K., et al., *Complex forearm deformities: operative strategy in posttraumatic pathology.* Obere Extremität, 2015. **10**(4): p. 229-239.
34. Nagy, L., L. Jankauskas, and C.E. Dumont, *Correction of forearm malunion guided by the preoperative complaint.* Clinical orthopaedics and related research, 2008. **466**(6): p. 1419.
35. Hoppenfeld, S., P. DeBoer, and R. Buckley, *Surgical exposures in orthopaedics: the anatomic approach*. 2012: Lippincott Williams & Wilkins.
36. Gaspar, M.P., et al., *Orthogonal plate fixation with corrective osteotomy for treatment of distal radius fracture malunion.* The Journal of hand surgery, 2017. **42**(1): p. e1-e10.
37. Dobbe, J.G., et al., *Patient-tailored plate for bone fixation and accurate 3D positioning in corrective osteotomy.* Medical & biological engineering & computing, 2013. **51**(1-2): p. 19-27.
38. Caiti, G., et al., *Computer-Assisted Techniques in Corrective Distal Radius Osteotomy Procedures.* IEEE reviews in biomedical engineering, 2019.
39. Walenkamp, M., et al., *Computer-assisted 3D planned corrective osteotomies in eight malunited radius fractures.* Strategies in Trauma and Limb Reconstruction, 2015. **10**(2): p. 109-116.
40. Bauer, A.S., et al., *Preoperative computer simulation and patient-specific guides are safe and effective to correct forearm deformity in children.* Journal of Pediatric Orthopaedics, 2017. **37**(7): p. 504-510.
41. Thomas, B.P. and R. Sreekanth, *Distal radioulnar joint injuries.* Indian journal of orthopaedics, 2012. **46**(5): p. 493.
42. Byrne, A.-M., et al., *Corrective osteotomy for malunited diaphyseal forearm fractures using preoperative 3-dimensional planning and patient-specific surgical guides and implants.* The Journal of hand surgery, 2017. **42**(10): p. 836. e1-836. e12.
43. Tack, P., et al., *3D-printing techniques in a medical setting: a systematic literature review.* Biomedical engineering online, 2016. **15**(1): p. 115.
44. Edmund, J.M. and T. Nyholm, *A review of substitute CT generation for MRI-only radiation therapy.* Radiation Oncology, 2017. **12**(1): p. 28.
45. Geldof, F., et al., *Comparing manual vertebral segmentation accuracy of MRI sequences with CT to find the imaging technique resulting in the best 3D segmentation for the SpineGuide.* Internship Technical Medicine, University of Twente, UMC Utrecht, May 2017: p. 19.
46. Florkow, M.C., et al., *3D CNN-based synthetic CT generation for head and neck radiotherapy using a clinically used turbo spin-echo T2-weighted sequence.* UMC Utrecht, Image Sciences Institue and Radiotheraphy Department, Utrecht, The Netherlands, 2018: p. 6.
47. Javaid, M. and A. Haleem, *Additive manufacturing applications in orthopaedics: a review.* Journal of clinical orthopaedics and trauma, 2018. **9**(3): p. 202-206.
48. van Eijnatten, M., et al., *CT image segmentation methods for bone used in medical additive manufacturing.* Medical engineering & physics, 2018. **51**: p. 6-16.
49. King, C. and W. Birch, *Assessment of maceration techniques used to remove soft tissue from bone in cut mark analysis.* Journal of forensic sciences, 2015. **60**(1): p. 124-135.
50. Rasband, W.S., *ImageJ, US National Institutes of Health, Bethesda, Maryland, USA.* https://imagej.nih.gov/ij/, 1997-2018.
51. LaValle, S.M., *Determining yaw, pitch, and roll from a rotation matrix.* Cambridge University Press, 2012.
52. Zhang, Z., *Iterative point matching for registration of free-form curves and surfaces.* International journal of computer vision, 1994. **13**(2): p. 119-152.
53. Landis, J.R. and G.G. Koch, *The measurement of observer agreement for categorical data.* biometrics, 1977: p. 159-174.
54. Bissinger, O., et al., *Micro-CT vs. whole body multirow detector CT for analysing bone regeneration in an animal model.* PloS one, 2016. **11**(11): p. e0166540.
55. Graham, T.J., *Surgical correction of malunited fractures of the distal radius.* JAAOS-Journal of the American Academy of Orthopaedic Surgeons, 1997. **5**(5): p. 270-281.
56. Aro, H.T. and T. Koivunen, *Minor axial shortening of the radius affects outcome of Colles' fracture treatment.* The Journal of hand surgery, 1991. **16**(3): p. 392-398.
57. Vroemen, J.C., et al., *Positioning evaluation of corrective osteotomy for the malunited radius: 3-D CT versus 2-D radiographs.* Orthopedics, 2013. **36**(2): p. e193-e199.

58. Kjer, H.M. and J. Wilm, *Evaluation of surface registration algorithms for PET motion correction*. 2010, Technical University of Denmark, DTU, DK-2800 Kgs. Lyngby, Denmark.
59. Reerink, J., et al., *Congenital anomalies in the first year of life in the Netherlands.* Nederlands Tijdschrift voor Geneeskunde, 1993. **137**: p. 504-509.
60. Boere-Boonekamp, M.M., et al., *Early detection of developmental dysplasia of the hip in The Netherlands: the validity of a standardized assessment protocol in infants.* American journal of public health, 1998. **88**(2): p. 285-288.
61. American Academy of Orthopaedic Surgeons. *Adolescent Hip Dysplasia*. Diseases & Conditions 2015 [cited 2019 01-10]; Available from: https://orthoinfo.aaos.org/en/diseases--conditions/adolescent-hip-dysplasia/.
62. Chan, A., et al., *Perinatal risk factors for developmental dysplasia of the hip.* Archives of Disease in Childhood-Fetal and Neonatal Edition, 1997. **76**(2): p. F94-F100.
63. Wilkin, G.P., et al., *A contemporary definition of hip dysplasia and structural instability: toward a comprehensive classification for acetabular dysplasia.* The Journal of arthroplasty, 2017. **32**(9): p. S20-S27.
64. Gala, L., J.C. Clohisy, and P.E. Beaulé, *Hip dysplasia in the young adult.* JBJS, 2016. **98**(1): p. 63-73.
65. Kerkar, P. *What causes adult hip dysplasia and how is it treated?* Hip pain 2018 [cited 2019 02-02]; Available from: https://www.epainassist.com/joint-pain/hip-pain/hip-dysplasia.
66. Moore, K.L., A.F. Dalley, and A.M. Agur, *Clinically oriented anatomy*. 6 ed. Lower Limb. 2009: Wolters Kluwer.
67. Staal, H., *Heupdysplasie*, in *De Baby Heup*, E. Humme, Editor. 2014, Universtiy Medical Centre Maastricht Post Academisch Onderwijs Geneeskunde - Orthopeadic Maastricht p. 27.
68. Korkmaz, Ö. and M. Malkoç, *Total Hip Replacement in Developmental Dysplasia of the Hip: Pitfalls and Challenges*, in *Developmental Diseases of the Hip-Diagnosis and Management*, D. Spasovski, Editor. 2017, InTechOpen. p. 114.
69. Huang, S., D. Zhao, and L. Yang, *New approach to the treatment of adolescent hip dysplasia.* Medical hypotheses, 2013. **81**(1): p. 122-124.
70. Bergmann, G., F. Graichen, and A. Rohlmann, *Hip joint loading during walking and running, measured in two patients.* Journal of biomechanics, 1993. **26**(8): p. 969-990.
71. Coronaphysio. *Hip joint labral tears*. Blog 2016 [cited 2019 02-02]; Available from: http://www.coronaphysio.net/hip-joint-labral-tears/.
72. Millis, M. and M. McClincy, *Periacetabular osteotomy to treat residual dysplasia in adolescents and young adults: indications, complications, results.* Journal of children's orthopaedics, 2018. **12**(4): p. 349-357.
73. Bankes, M.J.K. *Hip Dysplasia And PAO*. Specialist Hip Surgery for All Ages 2019 [cited 2019 02-02]; Available from: http://www.hipsurgery.london/hip-dysplasia-and-pao.
74. Dumont, G.D., R.D. Russell, and W.J. Robertson, *Anterior shoulder instability: a review of pathoanatomy, diagnosis and treatment.* Current reviews in musculoskeletal medicine, 2011. **4**(4): p. 200.
75. Afsari, A., *Anterior Glenohumeral Instability.* Academy of Orthopedic Surgeons, 2004. **79**(7): p. 311-6.
76. Sofu, H., et al., *Recurrent anterior shoulder instability: review of the literature and current concepts.* World Journal of Clinical Cases: WJCC, 2014. **2**(11): p. 676.
77. Dodson, C.C. and F.A. Cordasco, *Anterior glenohumeral joint dislocations.* Orthopedic Clinics of North America, 2008. **39**(4): p. 507-518.
78. Harvard University. *Shoulder Dislocation*. 2016 [cited 2019 10-01]; Available from: https://www.health.harvard.edu/a_to_z/shoulder-dislocation-a-to-z.
79. *Bankart Repair for Unstable Dislocating Shoulders*. Orthopaedics and Sports Medicine 2019 [cited 2019 02-02]; Available from: http://www.orthop.washington.edu/patient-care/articles/shoulder/bankart-repair-for-unstable-dislocating-shoulders.html.
80. Bliven, K.C.H. and G.P. Parr, *Outcomes of the Latarjet Procedure Compared With Bankart Repair for Recurrent Traumatic Anterior Shoulder Instability.* Journal of athletic training, 2018. **53**(2): p. 181-183.
81. Berg, B.V. and P. Omoumi, *Dislocation of the Shoulder Joint–Radiographic Analysis of Osseous Abnormalities.* Journal of the Belgian Society of Radiology, 2016. **100**(1).
82. Maquieira, G.J., C. Gerber, and A.G. Schneeberger, *Suprascapular nerve palsy after the Latarjet procedure.* Journal of shoulder and elbow surgery, 2007. **16**(2): p. e13-e15.
83. Willemsen, K., et al., *Een nieuwe behandeling voor heupdysplasie: een proof of concept.* Nederlandse Orthopaedsche Vereniging, 2018(UMC Utrecht).
84. Bartoníček, J., J. Vávra, and A. Chochola, *Bosworth hip shelf arthroplasty in adult dysplastic hips: ten to twenty three year results.* International orthopaedics, 2012. **36**(12): p. 2425-2431.
85. Miyasaka, D., et al., *Three-dimensional assessment of femoral head coverage in normal and dysplastic hips: a novel method.* Acta Medica Okayama, 2014. **68**(5): p. 277-284.
86. Willemsen, K., et al., *A novel treatment for anterior shoulder instability; A biomechanical comparison between a patient-specific implant and the Latarjet procedure*. 2019: To be publised in Journal of Bone & Joint Surgery.
87. Oldani, C. and A. Dominguez, *Titanium as a Biomaterial for Implants*, in *Recent advances in arthroplasty*, S. Fokter, Editor. 2012, InTechOpen.

88. Staiger, M.P., et al., *Magnesium and its alloys as orthopedic biomaterials: a review.* Biomaterials, 2006. **27**(9): p. 1728-1734.
89. Younger, E.M. and M.W. Chapman, *Morbidity at bone graft donor sites.* Orthopaedic Trauma, 1989. **3**(3): p. 192-195.
90. Baumhauer, J., et al., *Site selection and pain outcome after autologous bone graft harvest.* Foot & ankle international, 2014. **35**(2): p. 104-107.
91. Cypher, T.J. and J.P. Grossman, *Biological principles of bone graft healing.* The Journal of foot and ankle surgery, 1996. **35**(5): p. 413-417.
92. Amini, A.R., C.T. Laurencin, and S.P. Nukavarapu, *Bone tissue engineering: recent advances and challenges.* Critical Reviews in Biomedical Engineering, 2012. **40**(5).
93. Azimi, B., et al., *Poly (ε-caprolactone) fiber: an overview.* J Eng Fibers Fabr, 2014. **9**(3): p. 74.
94. Hutmacher, D.W., et al., *Mechanical properties and cell cultural response of polycaprolactone scaffolds designed and fabricated via fused deposition modeling.* Journal of Biomedical Materials Research: An Official Journal of The Society for Biomaterials, The Japanese Society for Biomaterials, and The Australian Society for Biomaterials and the Korean Society for Biomaterials, 2001. **55**(2): p. 203-216.
95. Hajiali, F., S. Tajbakhsh, and A. Shojaei, *Fabrication and properties of polycaprolactone composites containing calcium phosphate-based ceramics and bioactive glasses in bone tissue engineering: a review.* Polymer reviews, 2018. **58**(1): p. 164-207.
96. Radha, R. and D. Sreekanth, *Insight of magnesium alloys and composites for orthopedic implant applications–a review.* Journal of magnesium and alloys, 2017. **5**(3): p. 286-312.
97. Kim, J.A., et al., *Magnesium phosphate ceramics incorporating a novel indene compound promote osteoblast differentiation in vitro and bone regeneration in vivo.* Biomaterials, 2018. **157**: p. 51-61.
98. Castilho, M. and N. Golafshan, *Multi-process 3D (bio) printing for bone tissue regeneration* 2018, Department of Orthopeadics UMC Utrecht, Department of Biomedical Engineering Eindhoven University of Technology and Regenerative Medicine Center Utrecht p. 1-11.
99. Aarts, S., K. Willemsen, and R. Nizak, *Review on resorbable biomaterials for bone scaffold engineering and additive manufacturing*. 2018, Department of Ohopaedics UMC Utrecht.
100. Bergmann, G., et al., *Standardized loads acting in hip implants.* PloS one, 2016. **11**(5): p. e0155612.
101. Paul, J., *Force actions transmitted by joints in the human body.* Proceedings of the Royal Society of London. Series B, Biological Sciences, 1976: p. 163-172.
102. Bergmann, G., et al., *In vivo glenohumeral contact forces—measurements in the first patient 7 months postoperatively.* Journal of biomechanics, 2007. **40**(10): p. 2139-2149.
103. Nikooyan, A.A., *Forces in the Shoulder Joint: on validation of musculoskeletal shoulder models* 2012, Delft University of Technology and VU Vrije Universiteit. p. 49-70.
104. Benedetti, M., et al., *The effect of post-sintering treatments on the fatigue and biological behavior of Ti-6Al-4V ELI parts made by selective laser melting.* Journal of the mechanical behavior of biomedical materials, 2017. **71**: p. 295-306.
105. AMETEK Measurement and Calibration Technologies, *User Manual LS1, LS2.5 & LS5 Series Universal Test Machines*, in *LLoyd materials testing* 2013. p. 6.
106. Davis, J.R., *Tensile testing*. 2 ed. 2004, Ohio, USA ASM International. 283.
107. McVay Petre, B. *Trabecular and cancellous bone femur*. Osteology (Bone Anatomy) 2013 [cited 2019 02-02]; Available from: https://emedicine.medscape.com/article/1948532-overview.
108. Keaveny, T.M. and W.C. Hayes, *Mechanical properties of cortical and trabecular bone.* Bone, 1993. **7**: p. 285-344.

Appendices

Appendix A – ICP Algorithm

by Martin Kjer and Jakob Wilm, Technical University of Denmark, 2012 [58]

```
function [TR, TT, ER] = icp(q,p,varargin)
% Perform the Iterative Closest Point algorithm on three dimensional point
% clouds.
%
% [TR, TT] = icp(q,p)   returns the rotation matrix TR and translation
% vector TT that minimizes the distances from (TR * p + TT) to q.
% p is a 3xm matrix and q is a 3xn matrix.
%
% [TR, TT] = icp(q,p,k)   forces the algorithm to make k iterations
% exactly. The default is 10 iterations.
%
% [TR, TT, ER] = icp(q,p,k)   also returns the RMS of errors for k
% iterations in a (k+1)x1 vector. ER(0) is the initial error.
%
% [TR, TT, ER, t] = icp(q,p,k)   also returns the calculation times per
% iteration in a (k+1)x1 vector. t(0) is the time consumed for preprocessing.
%
% Additional settings may be provided in a parameter list:
% Boundary
%       {[]} | 1x? vector
%       If EdgeRejection is set, a vector can be provided that indexes into
%       q and specifies which points of q are on the boundary.
% EdgeRejection
%       {false} | true
%       If EdgeRejection is true, point matches to edge vertices of q are
%       ignored. Requires that boundary points of q are specified using
%       Boundary or that a triangulation matrix for q is provided.
% Extrapolation
%       {false} | true
%       If Extrapolation is true, the iteration direction will be evaluated
%       and extrapolated if possible using the method outlined by
%       Besl and McKay 1992.
% Matching
%       {bruteForce} | Delaunay | kDtree
%       Specifies how point matching should be done.
%       bruteForce is usually the slowest and kDtree is the fastest.
%       Note that the kDtree option is depends on the Statistics Toolbox
%       v. 7.3 or higher.
% Minimize
%       {point} | plane | lmaPoint
%       Defines whether point to point or point to plane minimization
%       should be performed. point is based on the SVD approach and is
%       usually the fastest. plane will often yield higher accuracy. It
%       uses linearized angles and requires surface normals for all points
%       in q. Calculation of surface normals requires substantial pre
%       proccessing.
%       The option lmaPoint does point to point minimization using the non
%       linear least squares Levenberg Marquardt algorithm. Results are
%       generally the same as in points, but computation time may differ.
% Normals
%       {[]} | n x 3 matrix
%       A matrix of normals for the n points in q might be provided.
%       Normals of q are used for point to plane minimization.
%       Else normals will be found through a PCA of the 4 nearest
%       neighbors.
% ReturnAll
%       {false} | true
%       Determines whether R and T should be returned for all iterations
%       or only for the last one. If this option is set to true, R will be
%       a 3x3x(k+1) matrix and T will be a 3x1x(k+1) matrix.
% Triangulation
%       {[]} | ? x 3 matrix
%       A triangulation matrix for the points in q can be provided,
%       enabling EdgeRejection. The elements should index into q, defining
%       point triples that act together as triangles.
% Verbose
%       {false} | true
%       Enables extrapolation output in the Command Window.
% Weight
%       {@(match)ones(1,m)} | Function handle
%       For point or plane minimization, a function handle to a weighting
%       function can be provided. The weighting function will be called
%       with one argument, a 1xm vector that specifies point pairs by
%       indexing into q. The weighting function should return a 1xm vector
```

```
%       of weights for every point pair.
% WorstRejection
%       {0} | scalar in ]0; 1[
%       Reject a given percentage of the worst point pairs, based on their
%       Euclidean distance.
%
% Martin Kjer and Jakob Wilm, Technical University of Denmark, 2012

% Use the inputParser class to validate input arguments.
inp = inputParser;

inp.addRequired('q', @(x)isreal(x) && size(x,1) == 3);
inp.addRequired('p', @(x)isreal(x) && size(x,1) == 3);
inp.addOptional('iter', 10, @(x)x > 0 && x < 10^5);
inp.addParameter('Precision', 4, @(x)x > -5 && x < 10);
inp.addParameter('Boundary', [], @(x)size(x,1) == 1);
inp.addParameter('EdgeRejection', false, @(x)islogical(x));
inp.addParameter('Extrapolation', false, @(x)islogical(x));
validMatching = {'bruteForce','Delaunay','kDtree'};
inp.addParameter('Matching', 'bruteForce', @(x)any(strcmpi(x,validMatching)));
validMinimize = {'point','plane','lmapoint'};
inp.addParameter('Minimize', 'point', @(x)any(strcmpi(x,validMinimize)));
inp.addParameter('Normals', [], @(x)isreal(x) && size(x,1) == 3);
inp.addParameter('NormalsData', [], @(x)isreal(x) && size(x,1) == 3);
inp.addParameter('ReturnAll', false, @(x)islogical(x));
inp.addParameter('Triangulation', [], @(x)isreal(x) && size(x,2) == 3);
inp.addParameter('Verbose', false, @(x)islogical(x));
inp.addParameter('Weight', @(x)ones(1,length(x)), @(x)isa(x,'function_handle'));
inp.addParameter('WorstRejection', 0, @(x)isscalar(x) && x > 0 && x < 1);
inp.parse(q,p,varargin{:});
arg = inp.Results;
clear('inp');
%%%%%%%%%%%%%%%%%%%%%%%%%%%%%%%%%%%%%%%%%%%%%%%%%%%%%%%%%%%%%%%%%%%%%%%%
% Actual implementation

% Allocate vector for time in every iteration.
%t = zeros(arg.iter+1,1);
% Start timer
Np = size(p,2);
% Transformed data point cloud
pt = p;
% Allocate vector for RMS of errors in every iteration.
%ER = zeros(arg.iter+1,1);
% Initialize temporary transform vector and matrix.
T = zeros(3,1);
R = eye(3,3);
% Initialize total transform vector(s) and rotation matric(es).
TT = zeros(3,1, 1);
TR = repmat(eye(3,3), [1,1,1]);

% If Minimize == 'plane', normals are needed
if (strcmp(arg.Minimize, 'plane') && isempty(arg.Normals))
    arg.Normals = lsqnormest(q,4);
end

% If Matching == 'Delaunay', a triangulation is needed
if strcmp(arg.Matching, 'Delaunay')
    DT = delaunayTriangulation(transpose(q));
end

% If Matching == 'kDtree', a kD tree should be built (req. Stat. TB >= 7.3)
if strcmp(arg.Matching, 'kDtree')
    kdOBJ = KDTreeSearcher(transpose(q));
end

% If edge vertices should be rejected, find edge vertices
if arg.EdgeRejection
    if isempty(arg.Boundary)
        bdr = find_bound(q, arg.Triangulation);
    else
        bdr = arg.Boundary;
    end
end

if arg.Extrapolation
    % Initialize total transform vector (quaternion ; translation vec.)
    qq = [ones(1,arg.iter+1);zeros(6,arg.iter+1)];
    % Allocate vector for direction change and change angle.
    dq = zeros(7,arg.iter+1);
    theta = zeros(1,arg.iter+1);
end
% Go into main iteration loop
```

```
for k=1:arg.iter

    % Do matching
    switch arg.Matching
        case 'bruteForce'
            [match, mindist] = match_bruteForce(q,pt);
        case 'Delaunay'
            [match, mindist] = match_Delaunay(q,pt,DT);
        case 'kDtree'
            [match, mindist] = match_kDtree(q,pt,kdOBJ);
    end

    % If matches to edge vertices should be rejected
    if arg.EdgeRejection
        p_idx = not(ismember(match, bdr));
        q_idx = match(p_idx);
        mindist = mindist(p_idx);
    else
        p_idx = true(1, Np);
        q_idx = match;
    end

    % If worst matches should be rejected
    if arg.WorstRejection
        edge = round((1-arg.WorstRejection)*sum(p_idx));
        pairs = find(p_idx);
        [~, idx] = sort(mindist);
        p_idx(pairs(idx(edge:end))) = false;
        q_idx = match(p_idx);
        mindist = mindist(p_idx);
    end

    if k == 1
        ER(k) = sqrt(sum(mindist.^2)/length(mindist));
    end

    switch arg.Minimize
        case 'point'
            % Determine weight vector
            weights = arg.Weight(match);
            [R,T] = eq_point(q(:,q_idx),pt(:,p_idx), weights(p_idx));
        case 'plane'
            weights = arg.Weight(match);
            [R,T] = eq_plane(q(:,q_idx),pt(:,p_idx),arg.Normals(:,q_idx),weights(p_idx));
        case 'lmaPoint'
            [R,T] = eq_lmaPoint(q(:,q_idx),pt(:,p_idx));
    end

    % Add to the total transformation
    TR(:,:,k+1) = R*TR(:,:,k);
    TT(:,:,k+1) = R*TT(:,:,k)+T;

    % Apply last transformation
    pt = TR(:,:,k+1) * p + repmat(TT(:,:,k+1), 1, Np);

    % Root mean of objective function
    ER(k+1) = rms_error(q(:,q_idx), pt(:,p_idx));

    % If Extrapolation, we might be able to move quicker
    if arg.Extrapolation
        qq(:,k+1) = [rmat2quat(TR(:,:,k+1));TT(:,:,k+1)];
        dq(:,k+1) = qq(:,k+1) - qq(:,k);
        theta(k+1) = (180/pi)*acos(dot(dq(:,k),dq(:,k+1))/(norm(dq(:,k))*norm(dq(:,k+1))));
        if arg.Verbose
            disp(['Direction change ' num2str(theta(k+1)) ' degree in iteration ' num2str(k)]);
        end
        if k>2 && theta(k+1) < 10 && theta(k) < 10
            d = [ER(k+1), ER(k), ER(k-1)];
            v = [0, -norm(dq(:,k+1)), -norm(dq(:,k))-norm(dq(:,k+1))];
            vmax = 25 * norm(dq(:,k+1));
            dv = extrapolate(v,d,vmax);
            if dv ~= 0
                q_mark = qq(:,k+1) + dv * dq(:,k+1)/norm(dq(:,k+1));
                q_mark(1:4) = q_mark(1:4)/norm(q_mark(1:4));
                qq(:,k+1) = q_mark;
                TR(:,:,k+1) = quat2rmat(qq(1:4,k+1));
                TT(:,:,k+1) = qq(5:7,k+1);
                % Reapply total transformation
                pt = TR(:,:,k+1) * p + repmat(TT(:,:,k+1), 1, Np);
                % Recalculate root mean of objective function
                % Note this is costly and only for fun!
                switch arg.Matching
```

```
                    case 'bruteForce'
                        [~, mindist] = match_bruteForce(q,pt);
                    case 'Delaunay'
                        [~, mindist] = match_Delaunay(q,pt,DT);
                    case 'kDtree'
                        [~, mindist] = match_kDtree(q,pt,kdOBJ);
                end
                ER(k+1) = sqrt(sum(mindist.^2)/length(mindist));
            end
        end
    end

    if abs(ER(k+1) - ER(k)) <= 10^-arg.Precision
        break
    end
end

if not(arg.ReturnAll)
    TR = TR(:,:,end);
    TT = TT(:,:,end);
end
%%%%%%%%%%%%%%%%%%%%%%%%%%%%%%%%%%%%%%%%%%%%%%%%%%%%%%%%%%%%%%%%%%%%%%%%%%%
function [match, mindist] = match_bruteForce(q, p)
    m = size(p,2);
    n = size(q,2);
    match = zeros(1,m);
    mindist = zeros(1,m);
    for ki=1:m
        d=zeros(1,n);
        for ti=1:3
            d=d+(q(ti,:)-p(ti,ki)).^2;
        end
        [mindist(ki),match(ki)]=min(d);
    end
mindist = sqrt(mindist);
%%%%%%%%%%%%%%%%%%%%%%%%%%%%%%%%%%%%%%%%%%%%%%%%%%%%%%%%%%%%%%%%%%%%%%%%%%%
function [match, mindist] = match_Delaunay(q, p, DT)
    match = transpose(nearestNeighbor(DT, transpose(p)));
    mindist = sqrt(sum((p-q(:,match)).^2,1));
%%%%%%%%%%%%%%%%%%%%%%%%%%%%%%%%%%%%%%%%%%%%%%%%%%%%%%%%%%%%%%%%%%%%%%%%%%%
function [match, mindist] = match_kDtree(~, p, kdOBJ)
    [match, mindist] = knnsearch(kdOBJ,transpose(p));
    match = transpose(match);
%%%%%%%%%%%%%%%%%%%%%%%%%%%%%%%%%%%%%%%%%%%%%%%%%%%%%%%%%%%%%%%%%%%%%%%%%%%
function [R,T] = eq_point(q,p,weights)
m = size(p,2);
n = size(q,2);
% normalize weights
weights = weights ./ sum(weights);
% find data centroid and deviations from centroid
q_bar = q * transpose(weights);
q_mark = q - repmat(q_bar, 1, n);
% Apply weights
q_mark = q_mark .* repmat(weights, 3, 1);
% find data centroid and deviations from centroid
p_bar = p * transpose(weights);
p_mark = p - repmat(p_bar, 1, m);
% Apply weights
%p_mark = p_mark .* repmat(weights, 3, 1);
N = p_mark*transpose(q_mark); % taking points of q in matched order
[U,~,V] = svd(N); % singular value decomposition
R = V*diag([1 1 det(U*V')])*transpose(U);
T = q_bar - R*p_bar;
%%%%%%%%%%%%%%%%%%%%%%%%%%%%%%%%%%%%%%%%%%%%%%%%%%%%%%%%%%%%%%%%%%%%%%%%%
function [R,T] = eq_plane(q,p,n,weights)

n = n .* repmat(weights,3,1);
c = cross(p,n);
cn = vertcat(c,n);
C = cn*transpose(cn);
b = - [sum(sum((p-q).*repmat(cn(1,:),3,1).*n));
       sum(sum((p-q).*repmat(cn(2,:),3,1).*n));
       sum(sum((p-q).*repmat(cn(3,:),3,1).*n));
       sum(sum((p-q).*repmat(cn(4,:),3,1).*n));
       sum(sum((p-q).*repmat(cn(5,:),3,1).*n));
       sum(sum((p-q).*repmat(cn(6,:),3,1).*n))];

X = C\b;
cx = cos(X(1)); cy = cos(X(2)); cz = cos(X(3));
sx = sin(X(1)); sy = sin(X(2)); sz = sin(X(3));
R = [cy*cz cz*sx*sy-cx*sz cx*cz*sy+sx*sz;
     cy*sz cx*cz+sx*sy*sz cx*sy*sz-cz*sx;
```

```
     -sy cy*sx cx*cy];

T = X(4:6);
%%%%%%%%%%%%%%%%%%%%%%%%%%%%%%%%%%%%%%%%%%%%%%%%%%%%%%%%%%%%%%%%%%%%%%%%%%
function [R,T] = eq_lmaPoint(q,p)
Rx = @(a)[1      0       0;
          0      cos(a)  -sin(a);
          0      sin(a)  cos(a)];
Ry = @(b)[cos(b)    0    sin(b);
          0         1    0;
          -sin(b)   0    cos(b)];
Rz = @(g)[cos(g)    -sin(g)  0;
          sin(g)    cos(g)   0;
          0         0        1];
Rot = @(x)Rx(x(1))*Ry(x(2))*Rz(x(3));

myfun = @(x,xdata)Rot(x(1:3))*xdata+repmat(x(4:6),1,length(xdata));
options = optimset('Algorithm', 'levenberg-marquardt');
x = lsqcurvefit(myfun, zeros(6,1), p, q, [], [], options);
R = Rot(x(1:3));
T = x(4:6);
%%%%%%%%%%%%%%%%%%%%%%%%%%%%%%%%%%%%%%%%%%%%%%%%%%%%%%%%%%%%%%%%%%%%%%%%%%
% Extrapolation in quaternion space. Details are found in:
%
% Besl, P., & McKay, N. (1992). A method for registration of 3-D shapes.
% IEEE Transactions on pattern analysis and machine intelligence, 239?256.
function [dv] = extrapolate(v,d,vmax)

p1 = polyfit(v,d,1); % linear fit
p2 = polyfit(v,d,2); % parabolic fit
v1 = -p1(2)/p1(1); % linear zero crossing
v2 = -p2(2)/(2*p2(1)); % polynomial top point

if issorted([0 v2 v1 vmax]) || issorted([0 v2 vmax v1])
    disp('Parabolic update!');
    dv = v2;
elseif issorted([0 v1 v2 vmax]) || issorted([0 v1 vmax v2])...
        || (v2 < 0 && issorted([0 v1 vmax]))
    disp('Line based update!');
    dv = v1;
elseif v1 > vmax && v2 > vmax
    disp('Maximum update!');
    dv = vmax;
else
    disp('No extrapolation!');
    dv = 0;
end
%%%%%%%%%%%%%%%%%%%%%%%%%%%%%%%%%%%%%%%%%%%%%%%%%%%%%%%%%%%%%%%%%%%%%%%%%%
% Determine the RMS error between two point equally sized point clouds with
% point correspondance.
% ER = rms_error(p1,p2) where p1 and p2 are 3xn matrices.
function ER = rms_error(p1,p2)
dsq = sum(power(p1 - p2, 2),1);
ER = sqrt(mean(dsq));
%%%%%%%%%%%%%%%%%%%%%%%%%%%%%%%%%%%%%%%%%%%%%%%%%%%%%%%%%%%%%%%%%%%%%%%%%%
% Converts (orthogonal) rotation matrices R to (unit) quaternion
% representations
%
% Input: A 3x3xn matrix of rotation matrices
% Output: A 4xn matrix of n corresponding quaternions
% http://en.wikipedia.org/wiki/Rotation_matrix#Quaternion
function quaternion = rmat2quat(R)

Qxx = R(1,1,:);
Qxy = R(1,2,:);
Qxz = R(1,3,:);
Qyx = R(2,1,:);
Qyy = R(2,2,:);
Qyz = R(2,3,:);
Qzx = R(3,1,:);
Qzy = R(3,2,:);
Qzz = R(3,3,:);
w = 0.5 * sqrt(1+Qxx+Qyy+Qzz);
x = 0.5 * sign(Qzy-Qyz) .* sqrt(1+Qxx-Qyy-Qzz);
y = 0.5 * sign(Qxz-Qzx) .* sqrt(1-Qxx+Qyy-Qzz);
z = 0.5 * sign(Qyx-Qxy) .* sqrt(1-Qxx-Qyy+Qzz);
quaternion = reshape([w;x;y;z],4,[]);
%%%%%%%%%%%%%%%%%%%%%%%%%%%%%%%%%%%%%%%%%%%%%%%%%%%%%%%%%%%%%%%%%%%%%%%%%%
% Converts (unit) quaternion representations to (orthogonal) rotation matrices R
%
% Input: A 4xn matrix of n quaternions
% Output: A 3x3xn matrix of corresponding rotation matrices
```

```
% http://en.wikipedia.org/wiki/Quaternions_and_spatial_rotation#From_a_quaternion_to_an_orthogonal_matrix
function R = quat2rmat(quaternion)
q0(1,1,:) = quaternion(1,:);
qx(1,1,:) = quaternion(2,:);
qy(1,1,:) = quaternion(3,:);
qz(1,1,:) = quaternion(4,:);

R = [q0.^2+qx.^2-qy.^2-qz.^2 2*qx.*qy-2*q0.*qz 2*qx.*qz+2*q0.*qy;
     2*qx.*qy+2*q0.*qz q0.^2-qx.^2+qy.^2-qz.^2 2*qy.*qz-2*q0.*qx;
     2*qx.*qz-2*q0.*qy 2*qy.*qz+2*q0.*qx q0.^2-qx.^2-qy.^2+qz.^2];
%%%%%%%%%%%%%%%%%%%%%%%%%%%%%%%%%%%%%%%%%%%%%%%%%%%%%%%%%%%%%%%%%%%%%%%%%%%
% Least squares normal estimation from point clouds using PCA
%
% H. Hoppe, T. DeRose, T. Duchamp, J. McDonald, and W. Stuetzle.
% Surface reconstruction from unorganized points.
% In Proceedings of ACM Siggraph, pages 71:78, 1992.
%
% p should be a matrix containing the horizontally concatenated column
% vectors with points. k is a scalar indicating how many neighbors the
% normal estimation is based upon.
% Note that for large point sets, the function performs significantly
% faster if Statistics Toolbox >= v. 7.3 is installed.
%
% Jakob Wilm 2010
function n = lsqnormest(p, k)
m = size(p,2);
n = zeros(3,m);
v = ver('stats');
if str2double(v.Version) >= 7.5
    neighbors = transpose(knnsearch(transpose(p), transpose(p), 'k', k+1));
else
    neighbors = k_nearest_neighbors(p, p, k+1);
end

for i = 1:m
    x = p(:,neighbors(2:end, i));
    p_bar = 1/k * sum(x,2);
    P = (x - repmat(p_bar,1,k)) * transpose(x - repmat(p_bar,1,k)); %spd matrix P
    %P = 2*cov(x);
    [V,D] = eig(P);
    [~, idx] = min(diag(D)); % choses the smallest eigenvalue
    n(:,i) = V(:,idx);   % returns the corresponding eigenvector
end
%%%%%%%%%%%%%%%%%%%%%%%%%%%%%%%%%%%%%%%%%%%%%%%%%%%%%%%%%%%%%%%%%%%%%%%%%%%
% Program to find the k - nearest neighbors (kNN) within a set of points.
% Distance metric used: Euclidean distance
%
% Note that this function makes repetitive use of min(), which seems to be
% more efficient than sort() for k < 30.
function [neighborIds, neighborDistances] = k_nearest_neighbors(dataMatrix, queryMatrix, k)

numDataPoints = size(dataMatrix,2);
numQueryPoints = size(queryMatrix,2);
neighborIds = zeros(k,numQueryPoints);
neighborDistances = zeros(k,numQueryPoints);
D = size(dataMatrix, 1); %dimensionality of points
for i=1:numQueryPoints
    d=zeros(1,numDataPoints);
    for t=1:D % this is to avoid slow repmat()
        d=d+(dataMatrix(t,:)-queryMatrix(t,i)).^2;
    end
    for j=1:k
        [s,t] = min(d);
        neighborIds(j,i)=t;
        neighborDistances(j,i)=sqrt(s);
        d(t) = NaN; % remove found number from d
    end
end
%%%%%%%%%%%%%%%%%%%%%%%%%%%%%%%%%%%%%%%%%%%%%%%%%%%%%%%%%%%%%%%%%%%%%%%%%%%
% Boundary point determination. Given a set of 3D points and a
% corresponding triangle representation, returns those point indices that
% define the border/edge of the surface.
function bound = find_bound(pts, poly)
%Correcting polygon indices and converting datatype
poly = double(poly);
pts = double(pts);
%Calculating freeboundary points:
TR = triangulation(poly, pts(1,:)', pts(2,:)', pts(3,:)');
FF = freeBoundary(TR);
%Output
bound = FF(:,1);
%%%%%%%%%%%%%%%%%%%%%%%%%%%%%%%%%%%%%%%%%%%%%%%%%%%%%%%%%%%%%%%%%%%%%%%%%%%
```

Appendix B – Statistics SPSS

The Cohen’s kappa measurement between observers (inter):

ALL_CT_CNK1HVU * ALL_MRI_CNK1HVU Crosstabulation

Count

		ALL_MRI_CNK1HVU										
		1,00	2,00	3,00	4,00	5,00	6,00	7,00	8,00	9,00	10,00	Total
ALL_CT_CNK1HVU	1,00	0	1	0	0	0	1	0	0	0	0	2
	2,00	1	2	0	0	2	0	0	0	0	0	5
	3,00	2	0	0	2	0	1	1	1	0	0	7
	4,00	0	0	2	1	1	1	0	0	0	0	5
	5,00	1	1	1	0	4	0	3	2	0	0	12
	6,00	0	2	1	3	1	6	5	4	0	0	22
	7,00	1	2	7	2	9	10	20	10	2	0	63
	8,00	0	0	2	0	4	5	18	19	6	0	54
	9,00	0	0	0	0	1	1	4	8	7	0	21
	10,00	0	0	0	0	0	0	0	0	0	1	1
Total		5	8	13	8	22	25	51	44	15	1	192

Symmetric Measures

		Value	Asymptotic Standard Error[a]	Approximate T[b]	Approximate Significance
Measure of Agreement	Kappa	,154	,041	4,805	,000
N of Valid Cases		192			

a. Not assuming the null hypothesis.

b. Using the asymptotic standard error assuming the null hypothesis.

The Cohen’s kappa measurement between 1 observer (intra):

Koen1 * Koen2 Crosstabulation

Count

		Koen2						
		4,00	5,00	6,00	7,00	8,00	9,00	Total
Koen1	5,00	1	1	0	0	0	0	2
	6,00	0	1	4	2	0	0	7
	7,00	0	0	2	10	7	0	19
	8,00	0	0	0	7	21	3	31
	9,00	0	0	0	0	1	4	5
Total		1	2	6	19	29	7	64

Symmetric Measures

		Value	Asymptotic Standard Error[a]	Approximate T[b]	Approximate Significance
Measure of Agreement	Kappa	,442	,091	5,728	,000
N of Valid Cases		64			

a. Not assuming the null hypothesis.

b. Using the asymptotic standard error assuming the null hypothesis.

Appendix C – Biodegradable hip/shoulder project

Appendix C.1 - Hip dysplasia

Every year, one to four children per 100 children are diagnosed with hip dysplasia in the Netherlands. [59, 60] Patients with hip dysplasia, also known as developmental dysplasia of the hip, have one or two underdeveloped hip joints. The hip joint consists of the femoral head (the ball) and the acetabulum (the socket) and together form a ball-socket joint. Hip dysplasia patients have a malposition of the femur head and/or a shallow acetabulum, see Figure 32. This abnormality leads to a chronic painful hip and invalidity. [61] In the Netherlands at birth and during infancy, children are screened for hip dysplasia. Risk factors for developing hip dysplasia are family history, female sex, breech position of the fetus and first-born children. [62] Patients are diagnosed by finding abnormal parameters on an anteroposterior radiographs of the pelvis. [63] When diagnosed before the age of 6 years with hip dysplasia, this abnormality can be 'naturally' corrected by pressing the femur in the acetabulum, for example with a fixed abduction splint ('gipsbroek'). Despite screening, several (young) adults with hip dysplasia are still undetected and then 'natural' correction is not possible anymore. [64]

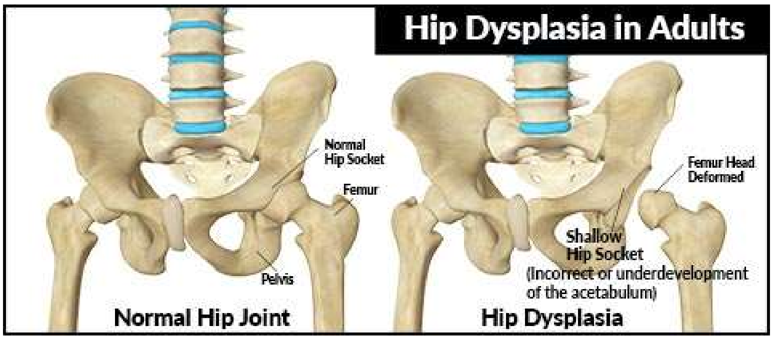

Figure 32: Anatomical models of the human pelvis with the femur ('ball') and acetabulum ('hip socket'). On the left a 'normal' hip joint and on the right a hip joint with hip dysplasia. [65]

Besides the bony femur and acetabulum, soft tissue around the hip joint is essential for its function. This soft tissue includes several muscles, cartilage and a fibrous capsule of ligaments (Figure 33). Among other functions, this capsule holds the femoral neck inside the acetabulum. [66]

Due to the abnormal hip joint anatomy of hip dysplasia patients, (sub)luxation occurs (Figure 32): The capsule and muscles cannot withstand these forces, resulting in displacement of the femoral head from the acetabular socket. Besides luxation, damage to the articular cartilage and the fibrocartilage ring, also known as the acetabular labrum, can be observed due to the increased and unevenly distributed mechanical stress. [61] In (young) adults this stress leads to the onset of osteoarthritis and eventually to the need of a total hip prothesis. [64] In the Netherlands, 29 percent of all total hip replacement-patients below the 60 are the result of hip dysplasia. [67] However, below the 60 years a total hip replacement is not recommended as primary treatment due to a high revision rate. [68] Therefore, when diagnosed with hip dysplasia as (young) adult, surgical treatment is recommended to correct the hip's malfunction and limit the damage in the hip joint. [69]

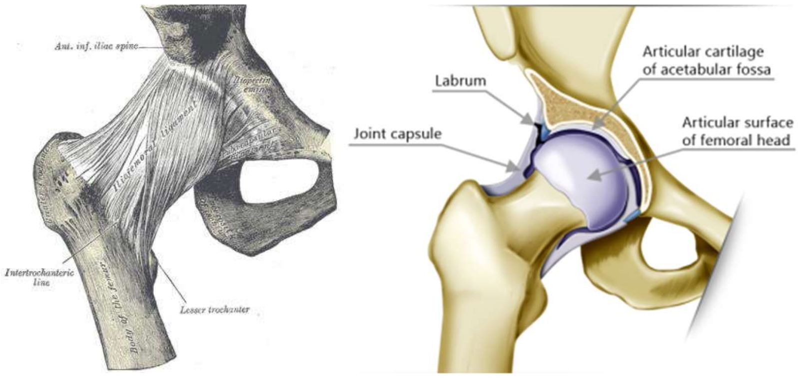

Figure 33: Anatomical figures of the hip ligament capsule. A) The outside ligaments of the hip joint are visualized [70]. B) On the right, the cartilage inside the capsule between the femur and acetabulum is displayed [71].

One of the most common surgical treatments is pelvic osteotomy. This procedure focusses on renewing articulation stability and decreasing unevenly distributed mechanical stress. The amount of reorientation, reshipment or salvage of the acetabulum or femoral head is patient-specific and is pre-operative determined by the orthopedic surgeon. [69] Most commonly a (Ganz) periacetabular osteotomy (PAO) is conducted as pelvic osteotomy, see Figure 34. PAO is a complex procedure and has a high complication rate: fifteen percent within the first ten weeks after surgery and 24 percent after a year. [72] The pelvic change could lead to overtreatment and a malcorrection of the hip deformity. Eventually these risks may lead to an impaired hip function, reoperations and destructive arthritis. [63]

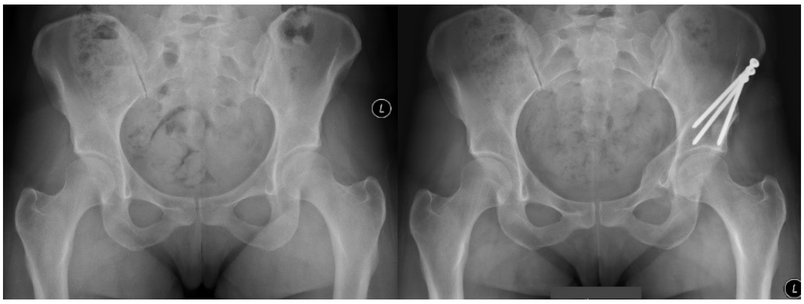

Figure 34: Anterior-posterior radiographs of a patient with hip dysplasia on the left hip (right on the image). The shallow acetabulum of the hip dysplasia can be seen on the left radiograph. On the right radiograph a PAO treatment is visible. [73]

Appendix C.2 - Anterior glenohumeral instability

A comparable disorder in another ball-socket joint is anterior glenohumeral instability. Anterior glenohumeral instability is a form of chronic shoulder instability and is seen in two percent of the general population. Men, enlisted people such as soldiers and contact athletes have high risk on developing shoulder instability. [74] Normally, the shoulder’s ball-socket joint consists of the humeral head (the ball) and the shallow glenoid fossa (the socket), see Figure 35. [75] Joint stability is established by the glenohumeral articulation, the labrum, glenohumeral ligaments, the rotator cuff muscles and the deltoid muscle. Due to a contact surface of 30 percent between the humeral head and the glenoid fossa, primary joint stability is realized by the surrounding soft tissue. [76] This results in the shoulder being the most mobile joint of the body, but unfortunately also in the most commonly dislocated joint. The amount of dislocation ranges from subtle laxity to recurrent dislocation and the most prevalent dislocation of glenohumeral instability is anterior. Besides a sharp pain in the arm, mostly during abduction and external rotation, the shoulder’s range of motion (ROM) is restricted in patients with shoulder instability. [77]

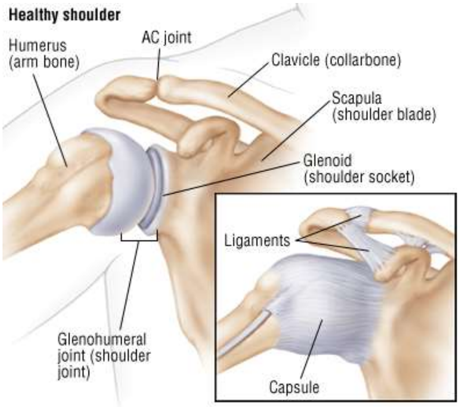

Figure 35: Anatomical overview of the shoulder joint, with the glenohumeral joint and its capsule enlarged. [78]

Shoulder instability is frequently the result of a traumatic injury and its consequence is often a lesion in the shoulder (Figure 36). Besides the Hill-Sachs lesion, a fracture of the humerus [77], the Bankart lesion is often seen. The Bankart lesion is the result of sufficient force on the anterior inferior glenoid labrum. As a result, part of the glenoid labrum detaches, leading to anterior instability. [76] Subsequently, recurrence of shoulder dislocation is seen in 90 percent of patients below 20 years, while patients older than 40 years have only a recurrence rate of ten percent. In addition, the recurrence risk is increased in patients who participate in contact and high-level sports if they are treated non-operatively. [74] A patient is diagnosed with shoulder instability based on the patient's history, abnormalities in a physical examination and a clinical evaluation on anterior, axillary lateral and scapular Y-view radiograph images. A Computerized Tomography (CT) and Magnetic Resonance Imaging (MRI) scan are used for further analysis of the joint, especially to find lesions such as capsular or labral damage. Without a suitable treatment, shoulder instability mostly leads to degenerative arthropathy of the shoulder joint and eventually to limitations in daily life. [76]

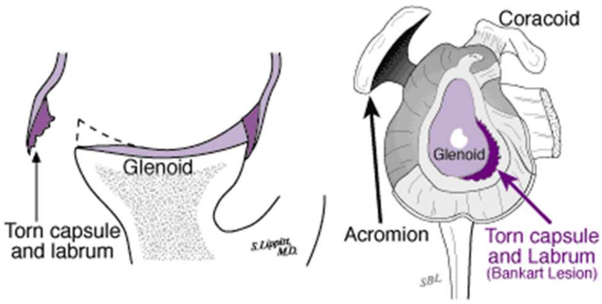

Figure 36: Anatomical overview of a Bankart lesion leading to anterior instability.[79]

Primary treatment aims to reduce the acute dislocation quickly and thereby reducing pain and restoring the ROM. With this, the arm will be placed in a sling and rest is recommended. With conservative treatment, patients below 25 years have a recurrence rate between 60 and 90 percent. Therefore, surgical treatment is considered for these patients. Surgical treatment is customized on the patient's intra-articular pathology and future lifestyle expectations. Two mainly used techniques are the Bankart repair and the Latarjet procedure. [74] The Bankart repair focusses on soft-tissue repair. With this repair, the anterior labral tear and anterior joint capsule are repaired by scraping the damaged anterior glenoid rim and inserting suture anchors. The Latarjet procedure is often applied for bony lesions or revisions, such as the detachment of glenoid labrum with a Bankart lesion (Figure 37). By splitting the subscapularis muscle, a window is created where the coracoid process bone or a autograft or allograft bone graft is transposed on the bony lesion. [80] Since 90 to 100 percent of the recurrent shoulder dislocation patients show a bony lesion, the Latarjet procedure is preferred for most patients with more than 20 percent glenoid bone loss. [76] Complications from the Latarjet procedure can range from mild (shoulder stiffness and loss of ROM) to severe, such as neurologic injury. [80] Furthermore, the used graft with the Latarjet procedure could collapse or resorb and are thus critical risk factors for this surgical procedure. [76] In addition, no current surgical treatment can guarantee the absence of dislocation recurrence. [74]

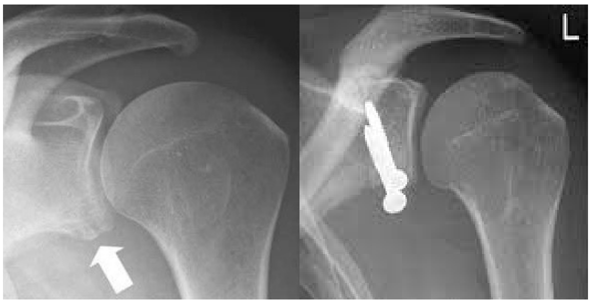

Figure 37: Radiographic overviews of the left shoulder joint. With on the left a left shoulder with a Bankart Lesion (arrow) [81]. On the right a shoulder after the Latarjet procedure, with two screws [82].

Appendix C.3 - Current research

Current surgical treatments for hip dysplasia and shoulder instability are not optimal. In addition, the anatomical deformations of the ball-socket joints are seen in every direction: sideways (sagittal), from the front to the back (coronal) and from head to toe (transversal) thus in 3D. By analyzing the deviation in 3D, the current research project in the UMC Utrecht emerged: a surgical treatment with a patient-specific 3D-printed titanium implant. [83]

For hip dysplasia this meant renewing the old-school shelf arthroplasty with a 3D-printed titanium implant. [83] With the former shelf arthroplasty operation, a shelf of mostly autologous bone is inserted extracapsular besides the acetabulum to increase the femoral head coverage, without changing the acetabular orientation. [84] The new approach uses a patient-specific 3D-printed titanium implant as shelf. With a pre-operative CT-scan and MRI-scan, a 3D hip analysis is created and among other things, the femoral coverage is measured. [85] With this information, the shape and size of the implant is determined. Eventually the implant is placed extracapsular with locking screws on the acetabulum (Figure 38). [83]

Figure 38: 3D model of the titanium hip implant, in this figure on the hip of a dog. [83]

For shoulder instability a similar potential treatment is proposed. The shoulder defect is filled with a patient-specific 3D-printed titanium implant. This implant is placed extracapsular directly on the glenoid bone in the defect and ideally has the size of the osteotomized glenoid rim, see Figure 39. In addition, as for hip dysplasia this implant is designed and created with a pre-operative CT- and MRI-scan. It is secured in the optimal position with locking screws. [86]

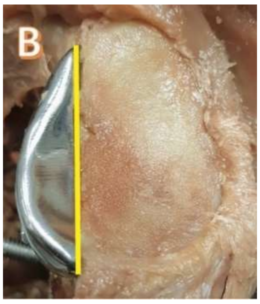

Figure 39: Lateral view of the glenoid with left the 3D-printed titanium patient-specific implant, placed on the defect. [86]

The patient-specific implants for hip dysplasia and anterior glenohumeral instability are seen in Figure 40.

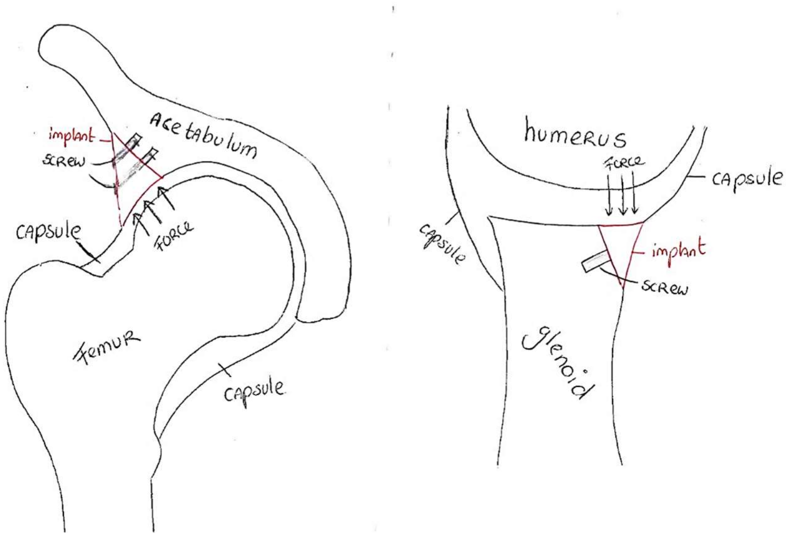

Figure 40: Overview sketches of the 3D-printed implants (red) for the hip (left) and shoulder (right).

Appendix C.4 – Problem definition & Research proposal biodegradable implant

These technologies seem promising, but research is required before it can be used in clinical practice. One of the drawbacks of the developed implant is the used material titanium. Although titanium is bioinert, the mechanical properties, such as the Young's modulus, between bone and titanium differ titanium is stiffer than the surrounding bone. No true adhesion between titanium and bone will be accomplished. Over time this results in wear, stress shielding and bone atrophy leading to implant loosening and eventually a possible revision surgery. [87]

A solution could be the use of a bone-like material. This material should have a more comparable Young's modulus to bone, be less stiff than titanium and therefore have a lower chance on a revision surgery. In addition, this material should allow bone grow inside the material to eventually become the patient's bone. [88] Using bone grafts (autograft or allograft) for this is disadvantageous due to the limited gathering, the possibility of tissue rejection and the limitation of the bone shape. [89-91] Therefore, a solution could be to use Bone Tissue Engineering (BTE). BTE aims to induce new functional bone regeneration via biomaterials. With BTE, a biodegradable bone-tissue material can be used to 3D print a patient-specific implant. This implant should provide temporary mechanical integrity until bone tissue is generated. [92] Eventually this implant should integrate in the patient's joint bone and the chance of revision surgery should be minimal. Different biodegradable materials could be used for this purpose, but the implant cannot break or provide other complications. Therefore, mechanical properties, biodegradability and other factors of promising biodegradable materials need to be analyzed.

A promising biodegradable material is poly-ε-caprolactone (PCL), a bioresorbable and biocompatible polymer. PCL has been approved by the Food and Drug Administration (FDA) for use in the human body and is already applied as biomaterial in biodegradable 3D scaffolds. Besides 3D processing in different shapes and structures, relative low costs, biocompatibility and high hydrolysis in the human body, PCL has a biodegradability suitable for long-term implant devices. [93] Despite these promising results, it is unsure if the mechanical properties of PCL are feasible for load-bearing applications. [94] Ideally the biodegradable scaffold material has similar mechanical properties to the surrounding bone. [95] In orthopedics, titanium has been used for centuries due to their high mechanical strength. To increase the mechanical strength of PCL, an added metallic may increase the mechanical strength of the composite. A promising biodegradable metallic material to add is Magnesium (Mg) [96], resulting in a composite scaffold of PCL with Mg, Strontium (Sr) and Phosphate (P): MgSrP. Magnesium (Mg) and Phosphate (P) are with Calcium the most important and common minerals in bone. Mg is besides biocompatible, biodegradable and bioresorbable, also light weighted and has a similar density and young's modulus of bone. Mg has a low corrosion resistance and a high hydrogen release during degradation, which accumulates in the surrounding soft tissue and has a negative effect on the Mg-implant. However, when Strontium (Sr) is used as alloy with Mg the alloy supports osteoblast growth, which builds bone tissue, and prevents bone resorption. In addition, it gains refinement and enhances Mg's corrosion resistance. [96] Furthermore, the alloy MgP shows an appropriate mechanical strength for bone repair. [97] When all combined, research of printed MgSrP-PCL, or MSP-PCL, manufactured with Fused Deposition Modelling (FDM) shows promising results, especially the ratio 70:30 (Appendix X.10 – Mechanical properties MgSrP-PCL). Recently, an in vitro evaluation of mesenchymal stem cells on with PCL and MSP-PCL was conducted. This study measured the metabolic and alkaline phosphatase activity as indication markers for bone formation and showed increased activity in MSP-PCL compared to PCL. In addition, an animal study with horses has just ended to analyze among other things the osseointegration and toxicity. In the coming months results will be made clear. For more information see Appendix X.10. [98]

This study focused on the potential bone-like biodegradable materials: PCL and MSP-PCL with a 30:70 ratio. Scaffolds of PCL and MSP-PCL will be obtained from researchers of the Department of Regenerative Medicine in Utrecht, the Netherlands. Both materials will be manufactured in two ways: printed with FDM (extrusion based) and casted.

The research questions is: *'Are the mechanical properties of the biodegradable PCL or MSP-PCL bone-like scaffold material sufficient to replace the porous titanium for the 3D-printed patient-specific implant for hip dysplasia and shoulder instability patients?*

The hypothesis of this study is that a biodegradable bone scaffold and corresponding structure with the desired properties can be found to replace the titanium material, with the wide available research in this field. A biodegradable bone-like 3D-printed patient-specific implant would improve the current treatment for hip dysplasia and shoulder instability. Eventually, if proven sufficient, this surgical treatment with biodegradable implant could replace the current treatments for hip dysplasia and shoulder instability.

Appendix C.5 Method and Materials

In this prospective study, the mechanical properties of PCL and MSP-PCL were investigated based on literature, previous research and a compression test. In addition, future tests to conducted were listed. For this, the desired mechanical properties for PCL and MSP-PCL were investigated. In Appendix X.8 the mechanical properties of bone are listed. With these information and known research materials [87, 94, 96, 99], a list of desired properties was made:

- Comparable requirements, to the currently used porous titanium scaffold:
  - Biocompatible; have no to minimal influence on the patients' healthcare.
  - Manufacturing with 3D printing; to create a patient-specific implant.
  - Osseointegration; a direct structural and functional connection between the surrounding bone and the surface of the load-bearing implant.
  - Pore size between 100 and 400 µm to allow cell growth and transportation of nutrients.
  - Withstand mechanical peak forces of 2880 to 3875 Newton (N) [100]; The hip is one of the most load bearing joints in the human body [101]. If the implant can withstand these peak forces, it can also withstand the forces of other joints. If too ambitious, the material should at least withstand mechanical peak forces of 1500 N (of the glenohumeral joint, around 150-180 percent of the body weight). [102, 103]
- Additional requirements, to outstand porous titanium:
  - Low in weight [96].
  - Less stiff than the porous titanium; a lower Young's Modulus than 110-113 gigapascal (GPa) [104] to prevent stress shielding of the implant and eventually implant failure.
  - A Young's Modulus to the surrounding cortical bone of 7-30 GPa to prevent mechanical failure when exposed joint load. This allows the patient to use the joint while bone is generated and bone remodeling is triggered by loading the site. [87]
  - The biodegradable implant should provide the required mechanical strength (as stated above) until the newly generated bone can take over;
    - Bioresorbable with controlled resorption rate matching the surrounding bone tissue, to maintain structure, prevent toxic reaction and wear. [94]
    - A controlled biodegradability; scaffolds retains its physical properties for at least 12 to 18 weeks; to allow bone tissue to replace the scaffold. [88]
  - Besides osseointegration also osteogenesis (bone ingrowth) and osteoconductive (scaffold serves as new bone growth to surrounding area with vital bone). [96]
  - Biodegradable material should not be toxic for surrounding tissue.[88]
  - Can be sterilized for medical use.

Study setup

To investigate these requirements, several mechanical tests were performed. This study investigated a compression test. In addition, a follow-up research investigated an additional compression test, a screw fixation test and biomechanical screw test. The PCL and MSP-PCL (70:30) scaffolds were similar produced by extrusion-based 3D printing (regenHU 3DDiscovery Evolution printer). The scaffolds were printed with a fiber thickness of 20 microns and an inter-fiber space of 1 millimeter or casted.

<u>Compression test</u>

To evaluate if PCL and MSP-PCL (70:30) withstand the maximum forces without flexing or breaking, their mechanical properties were analysed. Before the test, the samples were weighted, measured and put in a microCT. With the microCT, a porosity overview was made. In addition, the differences in weight (kilogram) and size (cm) can be measured to determine differences in manufacturing method. In a universal testing machine (AMETEK Lloyd Instruments Ltd, West Sussex, UK) visualized in Figuur 1, available at the Hogeschool Utrecht a compression test was conducted. For this test, three identical scaffolds of both material compositions were printed and casted resulting in 12 samples in total: 3 casted PCL, 3 printed PCL, 3 casted MSP-PCL and 3 printed MSP-PCL. All samples were a cylinder of 1x1x2 cm (diameter of 1 cm).

Figuur 1: Universal testing machine in the Hogeschool Utrecht. In this setup a tensile test is conducted. [105]

With the compression test, the maximum load on the biodegradable scaffold samples was tested. For this test, a sample was placed between the grips of the machine. With increasing load on the sample, the displacement of the sample is measured. With 1-2 mm per minute, a load of zero to 5000 N is placed on the sample. With the increasing load, the strain is displayed on the linked computer.

From the compression test, the compressive strength in MPa and a stress-strain curve was measured. With the tensile test, a stress-strain curve, the Young's modulus (GPa), yield stress (MPa) and ultimate tensile strength (MPa) were calculted. [106] The measured mechanical properties of PCL and MgSrP-PCL were compared to each other and to the mechanical properties of cortical bone (Appendix X.8), the gold standard, and porous titanium (Appendix X.9). In particular, the strain with the maximum hip joint load will be looked at. Ideally, the biodegradable materials will not plastically deform before the maximum joint load and their mechanical properties will be comparable with the human cortical bone.

Appendix C.6 Results

Figure 41 is an overview of the used samples for the compression test. The overall porosity differences can be seen here and in Figure 2. Both printed samples show more pores than the casted samples. In addition, the last sample in Figure 41 is misprinted.

Figure 41: The PCL samples casted and printed, followed by the MSP-PCL casted and printed samples. In addition, the last sample is a misprint of PCL.

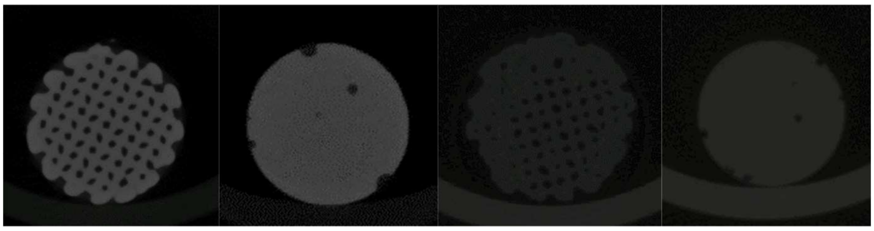

Figure 2: MicroCT samples from the MSP-PCL printed, MSP-PCL casted, PCL printed and PCL casted scaffold.

Figure 3 and 4 show the results from the compression test. Figure 3 and 4 show that the casted samples can withstand a higher stress with less strain. For results of follow-up tests including screw tests, see 'Report Bo Berends'.

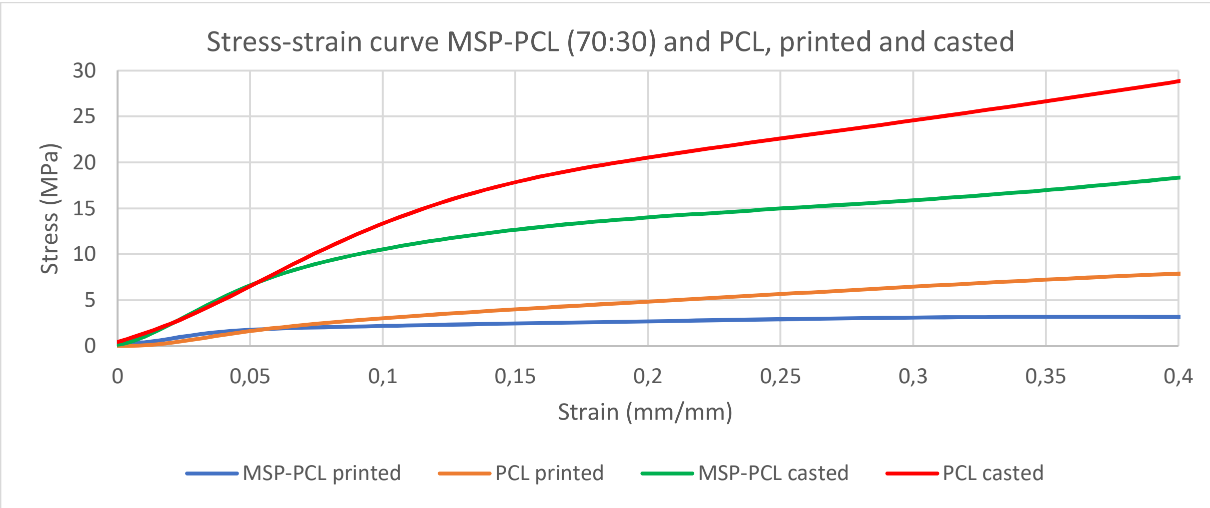

Figure 3: Stress-strain curve of MSP-PCL (70:30) and PCL from the compression test.

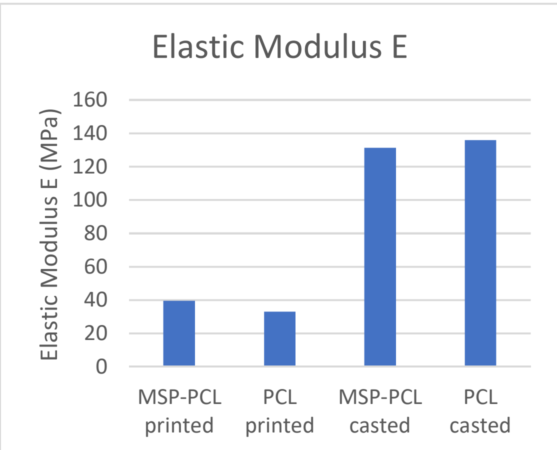

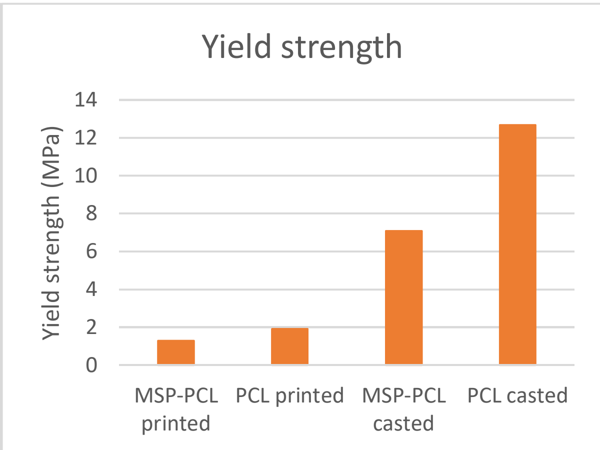

Figure 4: The elastic modulus E and yield strength derived from the stress-strain curve in Figure 3.

Appendix C.7 Discussion

With this short prospective study, the physical properties of two biodegradable materials were investigated to analyze if they can replace a titanium implant for shoulder instability and hip dysplasia. For this microCT's and a compression test were executed.

When looking at the different scaffold, the inconstant printing accuracy could be a problem for a 3D printed implant. The last scaffold in Figure 41 shows a misprint, which was visible more often. This is disadvantages when a constant quality is recommended. Moreover, the stress-strain curve in Figure 3 shows a different stress-strain curve from previous research {Castilho, 2018 #304}, but comparable to the second compression test from Bo Berends et al. However, these mechanical properties do go near the mechanical properties of cortical bone or titanium.

The microCT's showed many pores on the printed scaffold, but minimal pores on the casted scaffolds. Therefore, the casted scaffold does not meet the requirements for osseointegration and should not be used in this for as implant. However, the elastic modulus E and Yield strength of the casted scaffolds are higher and more towards the required properties. Therefore, a recommendation would be to analyze a porous coating if the casted for is preferred. This coating should then contain a porous material to allow osseointegration, such as a casted scaffold on the inside with a porous print on the outside.

When comparing the overall results from this study to the required properties, a lot of the requirements are not reached or investigated. Furthermore, the additional tests conducted by Bo Berends show that the mechanical properties of PCL and MSP-PCL might not suffice to be used as load-bearing implant. However, the biodegradable materials show great potential to be used as biodegradable implant. Therefore, a recommendation is to investigate is the scaffold structures that could help to meet the required mechanical properties. For example, a honeycomb structure or the inside of PCL and outside of MSP-PCL.

Another recommendation is to investigate other biodegradable materials to use for this purpose or even to use autologous graft to reshape as implant. With the known mechanical properties of bone, an autologous or donor bone graft could be meeting more requirements for this purpose.

For further research these recommendations need to be analyzed before PCL or MSP-PCL can be used further for 3D printed patient-specific load-bearing implants.

Appendix C.8 – Mechanical properties bone

The acetabulum and femur bone consist of cortical bone on the outside and cancellous or trabecular bone on the inside, see Figure 42.

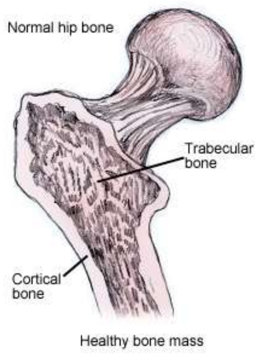

Figure 42: Section of a healthy femur, showing the cortical bone on the outside and cancellous or trabecular bone on the inside. [107]

Cortical bone is denser, harder and less porous than cancellous bone. This results in different mechanical properties, see Table 5 [99] and Figure 43.

Table 5: Mechanical properties cancellous and cortical bone. [99]

Material	Compressive strength (MPa)	Flexural strength (MPa)	Young's/Elastic modulus (GPa)	Porosity (%)	Strength test (MPa)
Cortical bone	100-230	50-150	7-30	3-12	27.5-42.3
Cancellous bone	2-12	10-20	0.1-5	50-90	-

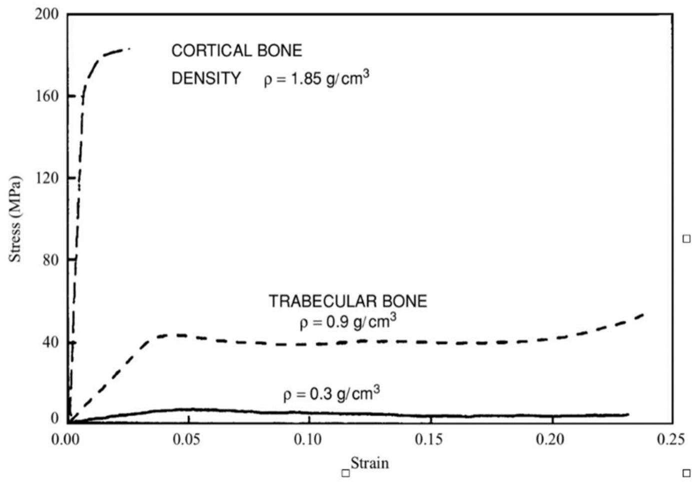

Figure 43: Stress-strain curve of cortical and cancellous or trabecular bone. [108]

Appendix C.9 – Mechanical properties porous titanium alloy Ti-6Al-4V

The already placed patient-specific implant was made of the porous titanium (Ti) alloy Ti-6Al-4V extra low interstitials (ELI) created with selective laser melting (SLM) as AM method. ELI improves ductility and increases the fracture toughness. For the composition of this alloy see Table 6. In Table 7 the mechanical properties are formulated. [104]

Table 6: Nominal chemical composition of the Ti-6Al-4V ELI alloy in weight percentage (wt%). [104]

Material	Ti	Al	V	O	N	C	H	Fe
%	Balance	5.5-6.75	3.5-4.5	< 0.13	< 0.05	< 0.08	< 0.012	< 0.25

Table 7: Mechanical properties of the Ti-6Al-4V ELI alloy. [104]

Material	Yield stress (MPa) – 0.2%	Ultimate tensile strength (MPa)	Young's/Elastic modulus (GPa)	Porosity (%)
Ti-6Al-4V	850-1015	960-1090	110-113	0.20-0.35

Appendix X.10 – Mechanical properties MgSrP-PCL

Sample scaffolds of MgSrP-PCL have been tested in several ratios. Their mechanical properties are shown in Figure 44.

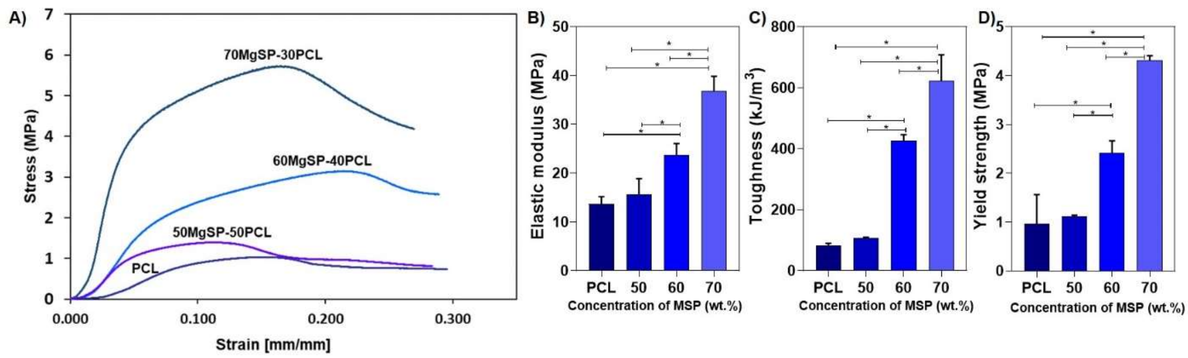

Figure 44: Mechanical properties of MgSrP-PCL with different ratios and PCL printed with FDM. On the left the stress-strain curve, on the right the elastic modulus (MPa), toughness (KJ/m^3) and Yield strength (MPa).